PROCEEDINGS A

royalsocietypublishing.org/journal/rspa

Research

Cite this article: Giraldo-Londoño O, Paulino GH. 2020 A unified approach for topology optimization with local stress constraints considering various failure criteria: von Mises, Drucker–Prager, Tresca, Mohr–Coulomb, Bresler– Pister and Willam–Warnke. *Proc. R. Soc. A* **476**: 20190861.
http://dx.doi.org/10.1098/rspa.2019.0861

Received: 11 December 2019
Accepted: 1 May 2020

Subject Areas:
computational mechanics, civil engineering, mechanical engineering

Keywords:
topology optimization, stress constraints, yield surface, material failure, augmented Lagrangian

Author for correspondence:
Glaucio H. Paulino
e-mail: paulino@gatech.edu

Dedicated to the memory of Prof. Daniel C. Drucker (1918–2001).

THE ROYAL SOCIETY
PUBLISHING

A unified approach for topology optimization with local stress constraints considering various failure criteria: von Mises, Drucker–Prager, Tresca, Mohr–Coulomb, Bresler–Pister and Willam–Warnke

Oliver Giraldo-Londoño and Glaucio H. Paulino

School of Civil and Environmental Engineering, Georgia Institute of Technology, Atlanta, GA 30332, USA

GHP, 0000-0002-3493-6857

An interesting, yet challenging problem in topology optimization consists of finding the lightest structure that is able to withstand a given set of applied loads without experiencing local material failure. Most studies consider material failure via the von Mises criterion, which is designed for ductile materials. To extend the range of applications to structures made of a variety of different materials, we introduce a unified yield function that is able to represent several classical failure criteria including von Mises, Drucker–Prager, Tresca, Mohr–Coulomb, Bresler–Pister and Willam–Warnke, and use it to solve topology optimization problems with local stress constraints. The unified yield function not only represents the classical criteria, but also provides a smooth representation of the Tresca and the Mohr–Coulomb criteria—an attribute that is desired when using gradient-based optimization algorithms. The present framework has been built so that it can be extended to failure criteria other than the ones addressed in this investigation. We present numerical examples to illustrate how the unified yield function can be used to obtain different designs, under prescribed loading or design-dependent loading (e.g. self-weight), depending on the chosen failure criterion.

1. Introduction

Given the design freedom it offers, topology optimization has become a powerful computational tool for the design of structural systems that are both efficient and organic. Within the field of topology optimization, stress-constrained topology optimization is known for being a challenging problem that still lacks a robust solution approach that is both efficient and suitable for large-scale applications. Part of the reason for the lack of such an approach is the nature of the problem itself. First, to solve the problem in a way that is consistent with continuum mechanics, one must treat stress as a local quantity, which in the context of topology optimization implies that a large number of stress constraints must be imposed to prevent material failure [1]. Second, it is known that the solution of a stress-constrained optimization problem lies on a degenerated region whose dimension is smaller than that of the solution space. Due to their degeneracy, traditional optimization techniques are unable to reach inside those regions, thus leading to sub-optimal designs [2–6].

A variety of approaches have been used to solve stress-constrained topology optimization problems, most of which are based on constraint aggregation techniques [7–19]. In those approaches, constraints are aggregated by means of a global stress function (e.g. the Kreisselmeier–Steinhauser [20] or the p-norm function [21]), which is used to approximate the maximum stress either in the entire design domain or in sub-regions. The global stress function estimates the maximum stress in the design domain, yet the quality of the estimation depends on the number of constraints that are aggregated and on the parameters of the aggregation function. As a result, the solution of the aggregated problem and that of the local problem differ. Besides aggregation, other approaches have been employed to solve stress-constrained topology optimization problems, yet instead of a complete literature survey, we revisit some of the most relevant studies related to this work and refer the reader to Senhora *et al.* [22] and the references therein for a comprehensive review of the stress-constrained literature.

The approach that we adopt in this study to solve stress-constrained topology optimization problems is based on the Augmented Lagrangian (AL) method [23,24]. This method is a numerical optimization technique that solves the original optimization problem with local constraints as the solution of a series of unconstrained optimization problems. It has been demonstrated that AL methods exhibit global convergence properties even for problems with degenerated constraints [25,26]. The method is gaining popularity in the topology optimization community and has been used since the mid-2000s to solve stress-constrained topology optimization problems [27,28]. More recently, this method has been adopted to solve stress-constrained topology optimization problems using the level-set method [29–31]. In the context of density-based topology optimization, the AL method has also been used to solve stress-constrained topology optimization problems considering loading uncertainties [32] or manufacturing uncertainties [33,34]. Although promising, these approaches use the AL method without any sort of normalization to avoid mesh dependency, which may not be conducive to the solution of large-scale topology optimization problems.

Aiming to solve large-scale problems, Senhora *et al.* [22] introduced a normalized AL-based approach for mass minimization topology optimization with local stress constraints. To enable the method to solve large-scale problems, they modify the AL function such that the penalty term is normalized with respect to the number of constraints, which prevents its unbounded growth as the number of stress constraints increases. *The normalization of the AL function allowed the method to solve problems with over one million local constraints*. An approach with such scalability attributes can ultimately make topology optimization a practical tool for engineering design, and thus we adopt it in the present study.

As in the approach by Senhora *et al.* [22], the vast majority of studies in the stress constraints literature use the von Mises failure criterion [35] to represent material failure. Although the von Mises criterion is useful to predict failure of ductile materials, a stress-based design using that criterion is not suitable for the design of structures manufactured using other types of materials with different strengths in tension and compression such as concrete, rock, soil, composites,

polymers, foams, among others. From the handful of studies considering stress constraints other than von Mises, the majority are based on the Drucker–Prager criterion (e.g. [36–39]). Besides the Drucker–Prager criterion, Duysinx *et al.* [40] considered the Rhagava [41] and Ishai [42] failure criteria, which consider different strengths in tension and compression. Other researchers such as Jeong *et al.* [43] and Yoon [44] considered various failure criteria, including Tresca [45], von Mises [35], Drucker–Prager [46] and Mohr–Coulomb [47], and used them to solve topology optimization problems with stress constraints.

In this study, we demonstrate that several classical failure criteria, including von Mises [35], Drucker–Prager [46], Tresca [45], Mohr–Coulomb [47], Bresler–Pister [48] and Willam–Warnke [49], can be represented by a single yield function, which we denote as the *unified yield function*. We use the unified yield function to define a general class of stress constraints that predicts failure of a variety of materials and use it to solve mass minimization topology optimization problems with local stress constraints. In addition to stress constraints, the formulation incorporates the effects of self-weight, which have a significant effect when the magnitude of the externally applied load is relatively small in comparison with the weight of the structure. To solve the problem with local constraints, we adopt an AL-based framework. Given the generality of the stress constraint, our formulation covers a spectrum of materials ranging from ductile metals to materials such as rocks, concrete, soils, polymeric foams, among others.

The ideation of this paper is motivated by the pioneering contributions of Professor Daniel C. Drucker to the field of applied mechanics, including his key contributions to the theory of plasticity [46,50–57]. His seminal contributions paved the way towards the development of a realistic theory of plasticity that has become useful in engineering applications. Our formulation for topology optimization is inspired by his fundamental work in the field, especially regarding the well-established Drucker–Prager yield criterion [46].

The remainder of this paper is organized as follows. In §2, we discuss the aforementioned classical yield functions and set the stage for the derivation of the unified yield function, which we present in detail in §3. Next, we introduce the stress-constrained topology optimization formulation in §4, followed by numerical results in §5. Finally, we provide some concluding remarks in §6. In addition to the aforementioned sections, we include the details of the sensitivity analysis in appendix A and provide a summary of the classical yield criteria, written in terms of the unified yield function, in appendix B.

2. Classical yield functions

We discuss several of the most popular yield criteria used in the engineering literature to predict failure of a variety of materials. The following discussion will set the stage to our derivation of the unified yield function, which we use to represent all failure criteria considered in this paper. Traditionally, a yield surface is expressed in terms of stress invariants as

$$f(I_1, J_2, J_3) = 0 \tag{2.1}$$

or in terms of principal stresses as

$$f(\sigma_1, \sigma_2, \sigma_3) = 0, \tag{2.2}$$

where

$$I_1 = \mathrm{tr}(\boldsymbol{\sigma}), \quad J_2 = \tfrac{1}{2}\mathbf{s}\colon \mathbf{s} \quad \text{and} \quad J_3 = \det(\mathbf{s}) \tag{2.3}$$

are, respectively, the first invariant of the Cauchy stress tensor, $\boldsymbol{\sigma}$, and the second and third invariants of the deviatoric stress tensor,

$$\mathbf{s} = \boldsymbol{\sigma} - \frac{I_1}{3}\mathbf{I}. \tag{2.4}$$

Without loss of generality, a yield surface described in the form given by either equation (2.1) or (2.2) can be written in normalized form as

$$\boxed{\Lambda = \sigma_{\text{eq}} - 1 = 0,} \tag{2.5}$$

where σ_{eq} is a (dimensionless) equivalent stress measure, which is defined in terms of either stress invariants or principal stresses. This form of writing the yield function leads to our generalization of local stress constraints in topology optimization. As will be discussed in the subsequent sections, the equivalent stress measure for many of the most popular yield criteria can be written in the following general form:

$$\boxed{\sigma_{\text{eq}} = \alpha(\theta)\sqrt{3J_2} + G(I_1),} \tag{2.6}$$

where $\alpha(\theta)$ is a function defined in terms of the Lode angle [58],

$$\theta = \frac{1}{3}\sin^{-1}\left(-\frac{3\sqrt{3}}{2}\frac{J_3}{J_2^{3/2}}\right), \quad -\frac{\pi}{6} \le \theta \le \frac{\pi}{6} \tag{2.7}$$

and $G(I_1)$ is a function defined in terms of the first stress invariant. The function $\alpha(\theta)$ is used to define the shape of the yield surface on the deviatoric plane and $G(I_1)$ is used to define the shape of the meridional section of the yield surface under triaxial stresses corresponding to $\theta = -\pi/6$.

(a) The von Mises and Drucker–Prager criteria

We begin by discussing the yield functions for the von Mises and Drucker–Prager criteria, which are defined in terms of stress invariants. The von Mises criterion is widely used to predict failure of ductile materials such as metals, while the Drucker–Prager criterion is typically used to predict failure of pressure-dependent materials such as soils, rocks or concrete. The von Mises yield criterion assumes that material failure occurs when the second deviatoric stress invariant reaches a critical value, and it is mathematically written as

$$f(J_2) = \sqrt{3J_2} - \sigma_{\text{lim}} = 0 \tag{2.8}$$

or in normalized form as

$$\Lambda(J_2) = \alpha\sqrt{3J_2} - 1 = 0, \tag{2.9}$$

with

$$\alpha = 1/\sigma_{\text{lim}}, \tag{2.10}$$

where σ_{lim} is the yield stress of the material. After comparing equation (2.9) with the normalized yield surface (2.5), the equivalent stress measure for the von Mises yield criterion is given by

$$\sigma_{\text{eq}} = \alpha\sqrt{3J_2}. \tag{2.11}$$

The Drucker–Prager yield criterion [46] not only depends on the second deviatoric stress invariant, but also on the first stress invariant (i.e. it is a pressure-dependent model). Using the form given by equation (2.5), the Drucker–Prager yield surface is written in normalized form as

$$\Lambda(I_1, J_2) = \alpha\sqrt{3J_2} + \beta I_1 - 1 = 0, \tag{2.12}$$

where

$$\alpha = \frac{\sigma_c + \sigma_t}{2\sigma_c\sigma_t} \quad \text{and} \quad \beta = \frac{\sigma_c - \sigma_t}{2\sigma_c\sigma_t} \tag{2.13}$$

and σ_c and σ_t are, respectively, the compressive and tensile strength of the material. When $\sigma_c = \sigma_t = \sigma_{\text{lim}}$, the values of α and β in equation (2.13) become $\alpha = 1/\sigma_{\text{lim}}$ and $\beta = 0$, meaning that the Drucker–Prager model reduces to the von Mises model when the tensile and compressive

strength of the material are the same. If one compares equations (2.12) and (2.5), it follows that the equivalent stress measure for the Drucker–Prager yield criterion is

$$\sigma_{\text{eq}} = \alpha\sqrt{3J_2} + \beta I_1. \tag{2.14}$$

Note that the equivalent stress measures for both the von Mises criterion (equation (2.11)) and the Drucker–Prager criterion (equation (2.14)) satisfy the general form given by equation (2.6).

(b) The Tresca and Mohr–Coulomb criteria

The Tresca and Mohr–Coulomb criteria, which are written in terms of principal stresses, are non-smooth versions of the von Mises and Drucker–Prager criteria, respectively. Assuming that the principal stresses are sorted such that $\sigma_1 \geq \sigma_2 \geq \sigma_3$, the normalized yield surface for the Tresca criterion is

$$\Lambda(\sigma_1, \sigma_2, \sigma_3) = \alpha(\sigma_1 - \sigma_3) - 1 = 0 \tag{2.15}$$

and for the Mohr–Coulomb criterion is

$$\Lambda(\sigma_1, \sigma_2, \sigma_3) = \alpha(\sigma_1 - \sigma_3) + \beta(\sigma_1 + \sigma_3) - 1 = 0, \tag{2.16}$$

where the value of α in equation (2.15) is that given by equation (2.10) and the values of α and β in equation (2.16) are those given by equation (2.13).[1]

Based on the forms in which the these yield criteria are written, it is not apparent that their corresponding equivalent stress measures, σ_{eq}, have the form shown in equation (2.6). In order to achieve the desired functional form of the equivalent stress measure, we express the Tresca and Mohr–Coulomb yield criteria in terms of stress invariants. For that purpose, we express the principal stresses in terms of stress invariants by means of the relationship [59]

$$\begin{bmatrix} \sigma_1 \\ \sigma_2 \\ \sigma_3 \end{bmatrix} = \frac{2}{\sqrt{3}}\sqrt{J_2}\begin{bmatrix} \sin\left(\theta + \frac{2\pi}{3}\right) \\ \sin(\theta) \\ \sin\left(\theta - \frac{2\pi}{3}\right) \end{bmatrix} + \frac{I_1}{3}\begin{bmatrix} 1 \\ 1 \\ 1 \end{bmatrix}. \tag{2.17}$$

Given that the Tresca criterion is a particular case of the Mohr–Coulomb criterion, the derivations below are shown for the Mohr–Coulomb model only. Substitution of equation (2.17) into equation (2.16) leads to an equivalent stress measure of the form

$$\sigma_{\text{eq}} = \hat{\alpha}(\theta)\sqrt{3J_2} + \hat{\beta} I_1, \tag{2.18}$$

where

$$\hat{\alpha}(\theta) = \frac{2}{3}(\sqrt{3}\alpha\cos\theta - \beta\sin\theta) \quad \text{and} \quad \hat{\beta} = \frac{2}{3}\beta. \tag{2.19}$$

For reasons that will become apparent later, we rewrite $\hat{\alpha}(\theta)$ as follows:

$$\hat{\alpha}(\theta) = \frac{2\alpha}{3}\sqrt{3 + (\beta/\alpha)^2}\cos(\theta + \tilde{\theta}), \quad \text{with } \tan\tilde{\theta} = \frac{\beta}{\alpha\sqrt{3}}. \tag{2.20}$$

Once again, note that the equivalent stress measure for the Tresca and Mohr–Coulomb models bears resemblance with the general form in equation (2.6).

It is known that these two failure criteria have non-differentiable regions, which may cause difficulties when using a gradient-based optimization algorithm. One way to overcome this issue is to round the vertices of the hexagon in the deviatoric plane for both failure criteria. As discussed

[1]The values of α and β are chosen such that Mohr–Coulomb and Drucker–Prager models predict the same strength in uniaxial tension and in uniaxial compression.

by Lagioia & Panteghini [60], rounding of the vertices can be achieved if we use a modified Lode angle of the form

$$\hat{\theta} = \tfrac{1}{3}\sin^{-1}(\zeta \sin 3\theta), \tag{2.21}$$

where $\zeta \leq 1$ is a rounding parameter. When $\zeta = 1$, then $\hat{\theta} = \theta$ and one recovers the original Tresca and Mohr–Coulomb models, but when $\zeta < 1$ one obtains a smoothed version of these two yield surfaces.

(c) The Bresler–Pister criterion

Another popular yield function, which is typically used to predict failure of isotropic materials such as concrete, polypropylene and polymeric foams, is the Bresler–Pister yield criterion [48]. In a normalized form, the Bresler–Pister yield surface is written as follows:

$$\Lambda(I_1, J_2) = \alpha_{\mathrm{BP}}\sqrt{3J_2} + \beta_{\mathrm{BP}} I_1 + \gamma_{\mathrm{BP}} I_1^2 - 1 = 0, \tag{2.22}$$

which corresponds to an equivalent stress measure,

$$\sigma_{\mathrm{eq}} = \alpha_{\mathrm{BP}}\sqrt{3J_2} + \beta_{\mathrm{BP}} I_1 + \gamma_{\mathrm{BP}} I_1^2, \tag{2.23}$$

where

$$\left.\begin{aligned} \alpha_{\mathrm{BP}} &= \frac{(\sigma_c + \sigma_t)\,(2 - \sigma_c/\sigma_b)\,(2 + \sigma_t/\sigma_b)}{\sigma_c\sigma_t\,(8 - 3\sigma_c/\sigma_b + \sigma_t/\sigma_b)}, \\ \beta_{\mathrm{BP}} &= \frac{(\sigma_c - \sigma_t)\,\left(4 - \sigma_c/\sigma_b - \sigma_t/\sigma_b + \sigma_c\sigma_t/\sigma_b^2\right)}{\sigma_c\sigma_t\,(8 - 3\sigma_c/\sigma_b + \sigma_t/\sigma_b)} \\ \text{and} \quad \gamma_{\mathrm{BP}} &= \frac{\sigma_c - 3\sigma_t + 2\sigma_c\sigma_t/\sigma_b}{\sigma_c\sigma_t\sigma_b\,(8 - 3\sigma_c/\sigma_b + \sigma_t/\sigma_b)}. \end{aligned}\right\} \tag{2.24}$$

Parameters σ_c, σ_t and σ_b are the yield stresses in uniaxial compression, uniaxial tension and equibiaxial compression, respectively. The Bresler–Pister criterion reduces to the Drucker–Prager criterion in the limit as $\sigma_b \to \infty$. That is because $\alpha_{\mathrm{BP}} \to (\sigma_c + \sigma_t)/(2\sigma_c\sigma_t)$, $\beta_{\mathrm{BP}} \to (\sigma_c - \sigma_t)/(2\sigma_c\sigma_t)$, and $\gamma_{\mathrm{BP}} \to 0$, when $\sigma_b \to \infty$, which if substituted into equation (2.23) yields the equivalent stress measure for the Drucker–Prager criterion given by equation (2.14).

(d) The Willam–Warnke criterion

In addition to the Bresler–Pister criterion, the Willam–Warnke criterion [49] has been used to predict failure in concrete and other cohesive-frictional materials. The normalized yield surface for the Willam–Warnke model is given by

$$\Lambda(I_1, J_2, \theta) = \frac{1}{\sigma_c}\sqrt{\frac{2}{15}}\frac{1}{r(\theta)}\sqrt{3J_2} + \beta_{\mathrm{W}} I_1 - 1 = 0 \tag{2.25}$$

which corresponds to

$$\sigma_{\mathrm{eq}} = \frac{1}{\sigma_c}\sqrt{\frac{2}{15}}\frac{1}{r(\theta)}\sqrt{3J_2} + \beta_{\mathrm{W}} I_1, \tag{2.26}$$

where $r(\theta)$ is given by

$$r(\theta) = \frac{u(\theta) + v(\theta)}{w(\theta)}, \tag{2.27}$$

and

$$\left.\begin{aligned} u(\theta) &= 2r_c(r_c^2 - r_t^2)\cos(\theta + \pi/6), \\ v(\theta) &= r_c(2r_t - r_c)\sqrt{4(r_c^2 - r_t^2)\cos^2(\theta + \pi/6) + 5r_t^2 - 4r_t r_c} \\ \text{and} \quad w(\theta) &= 4(r_c^2 - r_t^2)\cos^2(\theta + \pi/6) + (r_c - 2r_t)^2. \end{aligned}\right\} \tag{2.28}$$

Parameters r_c and r_t are expressed as

$$r_c = \sqrt{\frac{6}{5}}\frac{\sigma_b\sigma_t}{3\sigma_b\sigma_t + \sigma_c(\sigma_b - \sigma_t)} \quad \text{and} \quad r_t = \sqrt{\frac{6}{5}}\frac{\sigma_b\sigma_t}{\sigma_c(2\sigma_b + \sigma_t)}. \tag{2.29}$$

Finally, the parameter β_W is given by

$$\beta_W = \frac{\sigma_b - \sigma_t}{3\sigma_b\sigma_t}. \tag{2.30}$$

Convexity of the Willam–Warnke yield function requires that $r_t > r_c/2$.

The term $(1/\sigma_c)\sqrt{2/15}(1/r(\theta))$ that premultiplies $\sqrt{3J_2}$ in equation (2.26) can be rewritten as

$$\alpha(\theta) = \frac{A_W\cos^2(\theta + \pi/6) + B_W}{C_W\cos(\theta + \pi/6) + \sqrt{D_W\cos^2(\theta + \pi/6) + E_W}}, \tag{2.31}$$

where

$$\left.\begin{aligned} A_W &= \frac{4}{\sigma_c}\sqrt{\frac{2}{15}}(r_c^2 - r_t^2), \quad B_W = \frac{1}{\sigma_c}\sqrt{\frac{2}{15}}(r_c - 2r_t)^2, \quad C_W = 2r_c(r_c^2 - r_t^2), \\ D_W &= 4r_c^2(r_c - 2r_t)^2(r_c^2 - r_t^2), \quad E_W = r_c^2(r_c - 2r_t)^2(5r_t^2 - 4r_t r_c). \end{aligned}\right\} \tag{2.32}$$

If one sets $A_W \neq 0$, $C_W = 1$, and $B_W = D_W = E_W = 0$ the function $\alpha(\theta)$ above becomes $\alpha(\theta) = A_W\cos(\theta + \pi/6)$, which bears a striking resemblance to the function $\alpha(\theta)$ in equation (2.20) that was derived for the Tresca and Mohr–Coulomb criteria. Similarly, if one sets $A_W = C_W = D_W = 0$, $E_W = 1$, and $B_W \neq 0$, the function $\alpha(\theta)$ above becomes $\alpha(\theta) = B_W =$ constant, as is the case for the von Mises, Drucker–Prager, and Bresler–Pister criteria. This observation sheds some light on our development of a general form for $\alpha(\theta)$ that we use to define the unified yield function comprising all failure criteria discussed in this section. The specific form of the generalized yield function is provided next.

3. Unified yield function

The equivalent stress measure for all the yield criteria discussed in the previous section satisfies the general form given by equation (2.6). Particularly, the results show that all those yield criteria can be represented by a meridional function, $G(I_1)$, of the form given by a general polynomial of degree two and by a deviatoric function, $\alpha(\theta)$, of a form similar to that given by equation (2.31). Therefore, we unify all models discussed previously using one single yield function of the form shown in equation (2.5), such that the equivalent stress measure is given by[2]

$$\boxed{\sigma_{eq} = \hat{\alpha}(\theta)\sqrt{3J_2} + \hat{\beta}I_1 + \hat{\gamma}I_1^2,} \tag{3.1}$$

where the deviatoric function $\hat{\alpha}(\theta)$ is written as

$$\hat{\alpha}(\theta) = \frac{A\cos^2\hat{\theta} + B}{C\cos\hat{\theta} + \sqrt{D\cos^2\hat{\theta} + E}}, \tag{3.2}$$

with

$$\hat{\theta} = \tfrac{1}{3}\sin^{-1}[\zeta\sin 3\theta] + \bar{\theta}, \quad \zeta \leq 1. \tag{3.3}$$

A suitable choice of the parameters in equations (3.1)–(3.3) leads to each of the yield criteria discussed in the previous section. Table 1 provides a summary of the parameters that we use to represent all of these yield criteria.

As shown in figure 1, we use equation (3.1) with the parameters of table 1 to generate the yield surface for each of the classical models discussed in this paper. As observed in figure 1, the unified yield function is unable to smooth the apex of the Drucker–Prager, Mohr–Coulomb, Bresler–Pister and Willam–Warnke models, which may cause issues during topology optimization for cases in

[2]The unified yield function introduced here can be extended to accommodate other failure criteria such as Lade–Duncan [61] and Matsuoka–Nakai [62].

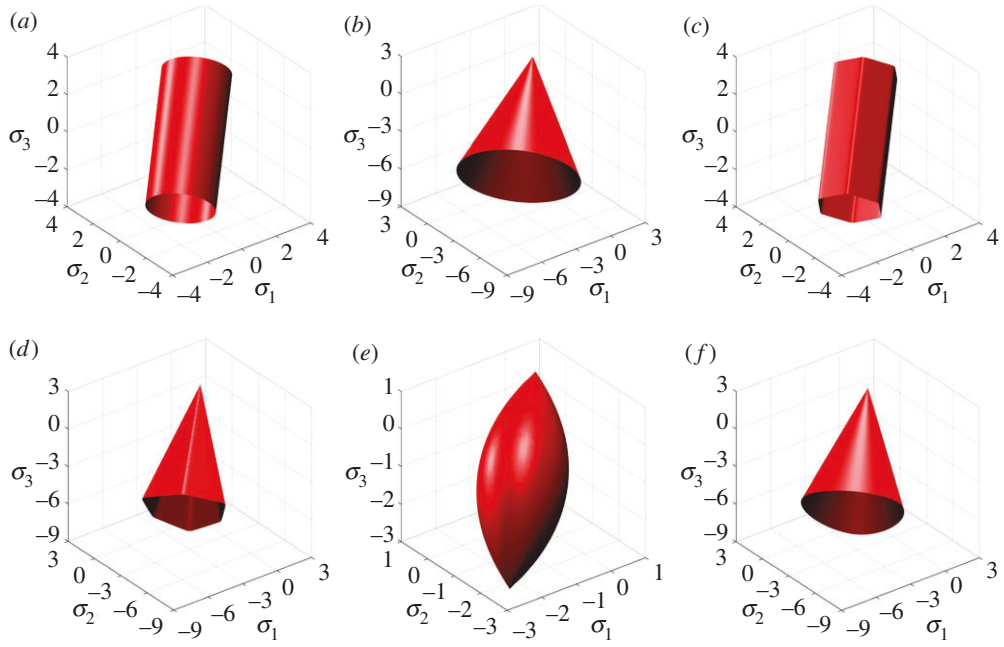

Figure 1. Yield surfaces obtained from the normalized yield function (2.5) using the equivalent stress measure given by equations (3.1)–(3.3): (*a*) von Mises, (*b*) Drucker–Prager, (*c*) Tresca, (*d*) Mohr–Coulomb, (*e*) Bresler–Pister, and (*f*) Willam–Warnke. The parameters used to generate these surfaces correspond to those from table 1 using $\sigma_{\text{lim}} = 1$, $\sigma_t = 0.5$, $\sigma_c = 1$, $\sigma_b = 1.25$ and $\zeta = 0.99$—for the Tresca and Mohr–Coulomb models. (Online version in colour.)

Table 1. Parameters defining the unified equivalent stress measure given by equations (3.1)–(3.3).

	$\hat{\alpha}(\theta)$								
failure criterion	A	B	C	D	E	ζ	$\bar{\theta}$	$\hat{\beta}$	$\hat{\gamma}$
von Mises	0	$\frac{1}{\sigma_{\text{lim}}}$	0	0	1	1	0	0	0
Drucker–Prager	0	$\frac{\sigma_c + \sigma_t}{2\sigma_c\sigma_t}$	0	0	1	1	0	$\frac{\sigma_c - \sigma_t}{2\sigma_c\sigma_t}$	0
Tresca	$\frac{2}{\sqrt{3}\sigma_{\text{lim}}}$	0	1	0	0	≤ 1[a]	0	0	0
Mohr–Coulomb[b]	A_{MC}	0	1	0	0	≤ 1[a]	$\tilde{\theta}$	$\frac{\sigma_c - \sigma_t}{3\sigma_c\sigma_t}$	0
Bresler–Pister[c]	0	α_{BP}	0	0	1	1	0	β_{BP}	γ_{BP}
Willam–Warnke[d]	A_{W}	B_{W}	C_{W}	D_{W}	E_{W}	1	$\frac{\pi}{6}$	$\frac{\sigma_b - \sigma_t}{3\sigma_b\sigma_t}$	0

[a] Setting $\zeta < 1$ leads to a yield surface with rounded corners [60].
[b] $A_{\text{MC}} = (2\alpha/3)\sqrt{3 + (\beta/\alpha)^2}$, in which α and β are given by equation (2.13), and $\tilde{\theta}$ is given by equation (2.20).
[c] α_{BP}, β_{BP} and γ_{BP} are given by equation (2.24).
[d] A_{W}, B_{W}, C_{W}, D_{W} and E_{W} are given by equation (2.32).

which the structure is subjected to purely hydrostatic loads. Although the apex can be smoothed using, for example, the approach by Abbo & Sloan [63], we decided not to include this feature because the issue happens under very specific circumstances.

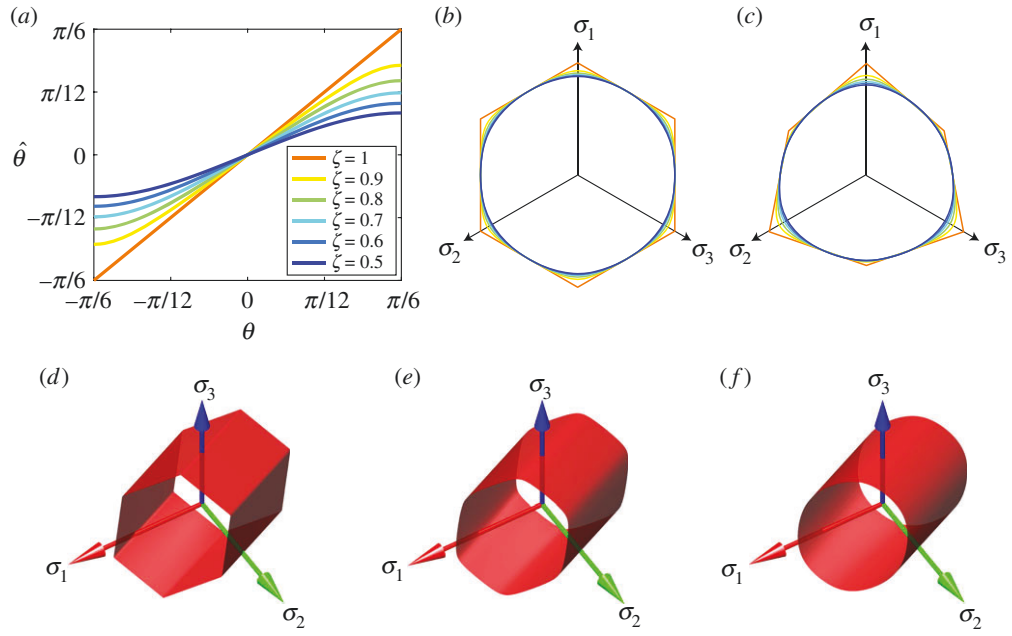

Figure 2. (*a*) Modified Lode angle, $\hat{\theta}$, computed using equation (3.3) for various values of rounding parameter ζ and for $\bar{\theta} = 0$. (*b*,*c*) The rounding parameter yields $\mathrm{d}\hat{\theta}/\mathrm{d}\theta = 0$ for $\theta = \pm\pi/6$, resulting on a smooth yield surface for the Tresca and Mohr–Coulomb models. (*d*–*f*) An illustration of the effect of rounding parameter ζ on the Tresca yield surface provided for $\zeta = 1$, 0.9 and 0.5, respectively. (Online version in colour.)

As we discussed in the preceding section, setting $\zeta < 1$ for the Tresca or Mohr–Coulomb models leads to yield surfaces with rounded corners on the deviatoric plane. Figure 2 shows the effect of the rounding parameter, ζ, on the modified Lode angle in equation (3.3) as well as its effect on the rounding of the Tresca yield surface. These results show that, as ζ decreases, the Tresca yield surface becomes more round and approaches a cylinder with circular cross section.

4. Topology optimization formulation

This section presents the general framework for topology optimization with local stress constraints considering the unified yield function introduced previously. The formulation aims to find the lightest structure that is able to withstand the applied loads without experiencing local material failure. To ensure that no material failure occurs, we impose local stress constraints, g_j, at a given number of evaluation points, K, throughout the design domain, Ω. We impose local constraints so that our formulation is consistent with classical continuum mechanics, which defines stress as a local quantity [64]. In a continuum setting, the topology optimization statement that we aim to solve is written as

$$\left.\begin{aligned} &\inf_{\rho\in\mathcal{A}} \quad m(\rho) \\ &\text{s.t.} \quad g_j(\rho,\mathbf{u}) \le 0, \quad j = 1,\ldots,K, \end{aligned}\right\} \tag{4.1}$$

where $m(\rho)$ is the mass (volume) of the structure normalized with respect to the total volume (mass) of domain Ω. The normalized mass is defined in terms of the density field, ρ, as

$$m(\rho) = \frac{1}{|\Omega|}\int_\Omega m_V(\rho)\,\mathrm{d}\mathbf{x}, \tag{4.2}$$

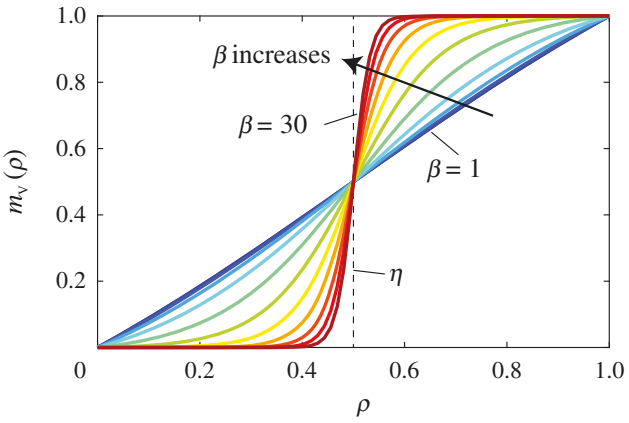

Figure 3. Threshold projection function (4.3) plotted for various values of β and for $\eta = 0.5$. As β increases, density values above η are projected to one and those below η are projected to zero. (Online version in colour.)

where $|\Omega|$ is the total mass (volume) of the structure and $m_V(\rho)$ is an interpolation function for the volume, which relates the density, ρ, at a point $\mathbf{x} \in \Omega$, with the volume fraction at that point. In this study, we define the volume interpolation function in terms of a threshold projection function, as follows [65]:

$$m_V(\rho) = \frac{\tanh(\beta\eta) + \tanh(\beta(\rho - \eta))}{\tanh(\beta\eta) + \tanh(\beta(1 - \eta))}, \tag{4.3}$$

where β controls the aggressiveness of the projection and η is a threshold value above which the density field is projected to one and below which it is projected to zero. Figure 3 depicts the threshold projection function for various values of β and for a value of $\eta = 0.5$.

For the topology optimization problem to be well defined, we restrict the density field to belong to a space of admissible density functions

$$\mathcal{A} = \left\{ \mathcal{P}_F(z) : z \in L^\infty(\Omega; [0,1]) \right\}, \tag{4.4}$$

defined by the regularization map

$$\mathcal{P}_F(z)(\mathbf{x}) = \int_\Omega F(\mathbf{x}, \bar{\mathbf{x}}) z(\bar{\mathbf{x}})\, \mathrm{d}\bar{\mathbf{x}}, \tag{4.5}$$

which is obtained via convolution with the nonlinear filter operator

$$F(\mathbf{x}, \bar{\mathbf{x}}) = c(\mathbf{x}) \max\left(1 - \frac{\|\mathbf{x} - \bar{\mathbf{x}}\|_2}{R}, 0\right)^q, \tag{4.6}$$

where $c(\mathbf{x})$ is chosen such that $\int_\Omega F(\mathbf{x}, \bar{\mathbf{x}})\, \mathrm{d}\bar{\mathbf{x}} = 1$, R is the filter radius, $\|\mathbf{x} - \bar{\mathbf{x}}\|_2$ is the Euclidean distance between points $\mathbf{x}$ and $\bar{\mathbf{x}}$, and $q \geq 1$ is a nonlinear filter exponent.[3]

Stress constraints $g_j(\rho, \mathbf{u})$ depend on the density field, ρ, and on the solution, $\mathbf{u} \in \mathcal{V}$, of the variational problem of nonlinear elasticity:[4]

$$\mathbf{u} = \inf_{\mathbf{u}} \left[\Pi(\rho, \mathbf{u}) + \frac{\epsilon}{2} \mathbf{u} \cdot \mathbf{u} \right], \tag{4.7}$$

in which ϵ is a Tikhonov regularization factor [66–68] and

$$\mathcal{V} = \{ \mathbf{u} \in H^1(\Omega, \mathbb{R}^3) : \mathbf{u}|_{\Gamma_D} = \mathbf{0} \} \tag{4.8}$$

[3]Other filter functions (e.g. linear hat filter, Gaussian filter, among others) can be used instead of that used in this study.

[4]We have added a Tikhonov regularization factor ϵ to the variational problem (4.7), to prevent the stiffness matrix from becoming singular when the density values become zero [66–68]. For implementation purposes, we use $\epsilon = 10^{-10}\text{mean}[\text{diag}(\mathbf{K}_T)]$, in which $\mathbf{K}_T$ is the stiffness matrix.

is the space of admissible displacement fields, where $\Gamma_D \in \partial\Omega$ is the portion of the boundary, $\partial\Omega$, in which zero displacements are prescribed (i.e. $\mathbf{u}|_{\Gamma_D} = \mathbf{0}$), and

$$\Pi(\rho, \mathbf{u}) = \int_\Omega m_E(\rho) W_0(\mathbf{u}, \mathbf{x}) \mathrm{d}\Omega - \int_\Omega m_V(\rho) \mathbf{b} \cdot \mathbf{u} \, \mathrm{d}\Omega - \int_{\Gamma_t} \mathbf{t} \cdot \mathbf{u} \, \mathrm{d}S \tag{4.9}$$

is the total potential energy of the system, where $m_E(\rho)$ is a stiffness interpolation function that relates the density ρ to the stiffness at a given point on the design domain, $W_0(\mathbf{u}, \mathbf{z})$ is the strain energy density of the solid material, $\mathbf{b}$ is the vector of body forces for $\rho = 1$, and $\mathbf{t}$ is the traction applied on $\Gamma_t \in \partial\Omega$. The boundaries Γ_D and Γ_t form a partition of $\partial\Omega$, such that $\Gamma_D \cup \Gamma_t = \partial\Omega$ and $\Gamma_D \cap \Gamma_D = \emptyset$. We use the following two stiffness interpolation functions in the present study:

$$m_E(\rho) = \tilde{\rho}^p \text{ (SIMP)} \quad \text{and} \quad m_E(\rho) = \frac{\tilde{\rho}}{1 + p_0(1 - \tilde{\rho})} \text{ (RAMP)}, \tag{4.10}$$

where $\tilde{\rho} = m_V(\rho)$, $p \geq 1$ is the SIMP penalization factor, and $p_0 \geq 0$ is the RAMP penalization factor. In the present study, we use SIMP [69–71], for cases in which self-weight is not considered and RAMP [72] otherwise. We use RAMP when considering self-weight because SIMP would lead to numerical instabilities that arise due to the fact that the weight-to-stiffness ratio becomes infinite when $\rho \to 0$, which leads to an unbounded displacement field [73]. The same type of numerical instabilities have been observed in stress-constrained topology optimization [18].

The equilibrium condition (4.7) is valid for any material with strain energy density, W_0. However, in order to keep the focus of this study on the unified yield function, we use a linear material whose stored energy function is given by

$$W_0 = \tfrac{1}{2} \varepsilon_{ij} C_{ijkl} \varepsilon_{kl}, \tag{4.11}$$

where ε_{ij} is the infinitesimal strain tensor and C_{ijkl} is the elasticity tensor for a linear isotropic material.

To find a numerical solution of the optimization problem (4.1), we discretize both the displacement and density fields. To obtain a discretized displacement field, we partition the design domain, Ω, into elements Ω_e, $e = 1, \ldots, N_e$, such that $\Omega = \bigcup_{e=1}^{N_e} \Omega_e$, and solve the variational problem (4.7) using the finite-element method. To discretize the density field, we assume a constant density value, ρ_e, in each element, Ω_e. Thus, the topology optimization statement in its discretized form becomes

$$\left.\begin{aligned} \min_{\mathbf{z}} \quad & m(\mathbf{z}) = \frac{1}{|\Omega|} \sum_{e=1}^{N_e} \tilde{\rho}_e v_e \\ \text{s.t.} \quad & g_j(\mathbf{z}, \mathbf{u}) \leq 0, \quad j = 1, \ldots, N_c \\ & 0 \leq z_e \leq 1, \quad e = 1, \ldots, N_e \\ \text{with:} \quad & \mathbf{u}(\mathbf{z}) = \arg\min_{\mathbf{u}} \left[\Pi(\mathbf{z}, \mathbf{u}) + \frac{\epsilon}{2} \mathbf{u}^T \mathbf{u} \right], \end{aligned}\right\} \tag{4.12}$$

where $\mathbf{z}$ are the design variables, $\mathbf{z} \mapsto \mathbf{u}(\mathbf{z})$ is an implicit function of the design variables that we define through the equilibrium condition shown in $(4.12)_4$, $\tilde{\rho}_e = m_V(\rho_e)$ represents the volume (mass) fraction of element e, and $v_e = |\Omega_e|$ is the volume of solid element, e. The discrete density values, ρ_e, are defined in a discrete form via a regularization filter, which we obtain by discretization of equations (4.5)–(4.6). The vector of filtered density values is obtained as

$$\boldsymbol{\rho}(\mathbf{z}) = \mathbf{P}\mathbf{z}, \tag{4.13}$$

where

$$P_{ij} = \frac{w_{ij} v_j}{\sum_{k=1}^{N_e} w_{ik} v_k} \tag{4.14}$$

is the filter matrix, defined in terms of the nonlinear filter function,

$$w_{ij} = \max\left(1 - \frac{\|\mathbf{x}_i - \mathbf{x}_j\|_2}{R}, 0\right)^q, \tag{4.15}$$

where $\|\mathbf{x}_i - \mathbf{x}_j\|_2$ represents the distance between the centroids, $\mathbf{x}_i$ and $\mathbf{x}_j$, of elements i and j, respectively. Note that setting $q = 1$ in equation (4.15) leads to the traditional linear hat filter [74].

We evaluate the total potential energy as

$$\Pi(\mathbf{z}, \mathbf{u}) = \sum_{e=1}^{N_e} \int_{\Omega_e} m_E(\rho_e) W_0(\mathbf{u}_e)\, \mathrm{d}\Omega - \mathbf{f}_{\text{ext}}^T \mathbf{u}, \tag{4.16}$$

where $\mathbf{u}$ is the vector of nodal displacements and

$$\mathbf{f}_{\text{ext}} = \mathbf{f}_n + \mathbf{f}_b \tag{4.17}$$

is the vector of external forces, which is composed of the vector of nodal forces, $\mathbf{f}_n$ (due to the external traction, $\mathbf{t}$) and the vector of body forces, $\mathbf{f}_b$ (e.g. due to gravity). We assume that the external traction is independent of the design variables, and thus the vector of nodal forces is also independent of the design variables. However, due to gravitational forces, the vector of body forces inherently depends on the design variables. In a finite-element implementation, the vector of nodal forces and that of body forces are evaluated for each finite element, e, as follows:

$$\mathbf{f}_n^e = \int_{\Gamma_t^e} \mathbf{N}_e^T \mathbf{t}\, \mathrm{d}S, \quad \mathbf{f}_b^e = \int_{\Omega_e} m_V(\rho_e) \mathbf{N}_e^T \mathbf{b}\, \mathrm{d}\Omega, \tag{4.18}$$

where $\mathbf{N}_e$ is the vector of shape functions for element e, and $\mathbf{b} = \gamma \hat{\mathbf{n}}$ is the vector of body forces, in which γ is the specific weight of the solid material and $\hat{\mathbf{n}}$ is a unit vector in the direction of gravity (e.g. $\hat{\mathbf{n}} = [0\ 0\ -1]^{\mathrm{T}}$). The term $m_V(\rho_e)$ in equation $(4.18)_2$ clearly shows the explicit dependence of the vector of external forces on the design variables.

(a) Polynomial vanishing constraint

We introduce a new type of stress constraint, which we denote to as *polynomial vanishing constraint*. This constraint is a variation of the traditional vanishing constraint used in topology optimization and is defined as

$$\boxed{g_j(\mathbf{z}, \mathbf{u}) = m_E(\rho_j) \Lambda_j (\Lambda_j^2 + 1), \quad \text{with } \Lambda_j = \sigma_j^{\text{eq}} - 1,} \tag{4.19}$$

where σ_j^{eq} is the unified equivalent stress measure computed from equations (3.1)–(3.3) using the stresses obtained at evaluation point $\mathbf{x}_j$, $j = 1 \ldots, N_c$. For the present study, we consider one evaluation point per element corresponding to its centroid.

The benefits of using the polynomial vanishing constraint (4.19) are twofold. First, when $\sigma_j^{\text{eq}} \gg 1$, the constraint is dominated by the cubic term, Λ_j^3, i.e. $g_j(\mathbf{z}, \mathbf{u}) \propto (\sigma_j^{\text{eq}} - 1)^3$, and, as a result, the optimizer will drive the solution to a density distribution with overall lower stress, thus speeding up the convergence towards stress constraint satisfaction. Second, as the constraints are close to being active (i.e. when $\sigma_j^{\text{eq}} \to 1$), the constraint is dominated by the linear term, Λ_j, meaning that the polynomial vanishing constraint behaves as a traditional vanishing constraint [75].

(b) Normalized Augmented Lagrangian

We use an AL-based method to solve the optimization statement (4.12). In the traditional AL method [23,24], the original problem is replaced by a series of unconstrained optimization problems that eventually converge to the solution of the original problem. At the kth step, one seeks to find the minimizer of the AL function[5]

$$J^{(k)}(\mathbf{z}) = \frac{1}{|\Omega|} \sum_{e=1}^{N_e} \tilde{\rho}_e v_e + \sum_{j=1}^{N_c} \left[\lambda_j^{(k)} h_j(\mathbf{z}, \mathbf{u}) + \frac{\mu^{(k)}}{2} h_j(\mathbf{z}, \mathbf{u})^2 \right], \tag{4.20}$$

[5]In practice, we find an approximate minimizer of the AL function by running a few MMA iterations per AL step. The number of iterations that we use is typically $N_{\text{MMA}} = 5$.

where the first term, denoted as the objective function term, corresponds to the objective function in (4.12), and the second term, denoted as the penalty term, contains the stress constraints. The terms $h_j(\mathbf{z}, \mathbf{u})$ in equation (4.20) are given by

$$h_j(\mathbf{z}, \mathbf{u}) = \max\left[g_j(\mathbf{z}, \mathbf{u}), -\frac{\lambda_j^{(k)}}{\mu^{(k)}}\right], \quad \forall j = 1, \ldots, N_c, \tag{4.21}$$

where $\lambda_j^{(k)}$ are Lagrange multiplier estimators and $\mu^{(k)}$ is a penalty factor. For a detailed derivation of the expression for $h_j(\mathbf{z}, \mathbf{u})$ in equation (4.21), the reader is referred to the work by Senhora *et al.* [22]. Both the Lagrange multiplier estimators and the penalty factor are updated at each AL step as follows:

$$\lambda_j^{(k+1)} = \lambda_j^{(k)} + \mu^{(k)} h_j(\mathbf{z}^{(k)}, \mathbf{u}), \quad \forall j = 1, \ldots, N_c \tag{4.22}$$

and

$$\mu^{(k+1)} = \min[\alpha \mu^{(k)}, \mu_{\max}], \tag{4.23}$$

where $\alpha > 1$ is the penalty update parameter and $\mu_{\max}$ is a maximum value of the penalty factor used to prevent ill-conditioning during the optimization steps.

Our experience has shown that, as the number of elements in the finite-element mesh increases (i.e. as the number of stress constraints increases), the solution of the kth sub-problem becomes dominated by the penalty term of the AL function, which negatively impacts the convergence of the method towards a solution of (4.12). To improve the ability of the AL method to solve problems with increasing number of constraints, we normalize the penalty term of the AL function with respect to the number of constraints. This adjustment significantly improves the ability of the method to solve problems with a large number of constraints [22]. The normalized AL function is given by

$$J^{(k)}(\mathbf{z}) = \frac{1}{|\Omega|}\sum_{e=1}^{N_e} \tilde{\rho}_e v_e + \frac{1}{N_c}\sum_{j=1}^{N_c}\left[\lambda_j^{(k)} h_j(\mathbf{z}, \mathbf{u}) + \frac{\mu^{(k)}}{2} h_j(\mathbf{z}, \mathbf{u})^2\right]. \tag{4.24}$$

To solve the stress-constrained topology optimization problem, we use the AL method yet instead of minimizing (4.20) at each step k, we minimize the normalized function (4.24). We require the sensitivity of the normalized AL function with respect to the design variables to find the minimizer of (4.24) at each AL step. For the sensitivity analysis, one must consider the implicit dependence of $J^{(k)}(\mathbf{z})$ on the solution, $\mathbf{u}$, of the boundary value problem, as we show in detail in appendix A.

5. Numerical results

We present two numerical examples to illustrate the capabilities of the proposed formulation to handle different yield criteria by means of the unified yield function and to study the effect of self-weight in the optimization results. Unless otherwise specified, we use the set of initial parameters shown in table 2 to solve both problems.

The unified yield function introduced previously is able to represent several classical failure criteria defined for a variety of materials (e.g. for ductile metals, concrete, ceramics, polymeric foams, among others). Thus, the numerical examples discussed below aim to find optimized topologies of structures that can be fabricated with materials whose failure behaviour can be represented by the unified yield function. Specifically, the examples discussed herein consider structures that can be fabricated with either a metal or a concrete-like material. For structures made of metals, we choose $E = 200\,\text{GPa}$ and $\nu = 0.3$ (i.e. elastic properties of steel) and a yield stress, $\sigma_{\text{lim}} = 250\,\text{MPa}$. For structures made of a concrete-like material, we choose a Young's modulus, $E = 30\,\text{GPa}$, a Poisson's ratio, $\nu = 0.2$, and yield stresses that depend on the yield criterion of choice (e.g. for Drucker–Prager or Mohr–Coulomb we define values for σ_t and σ_c, and for Bresler–Pister or Willam–Warnke we define values for σ_t, σ_c and σ_b).

Table 2. Input parameters used to solve all examples.

parameter	value
initial Lagrange multiplier estimators, $\lambda_j^{(0)}$	0
initial penalty factor, $\mu^{(0)}$	10
maximum penalty factor, $\mu_{\max}$	10 000
penalty factor update parameter, α	1.05
SIMP penalization factor, p[a]	3
RAMP penalization factor, p_0[a]	3.5
nonlinear filter exponent, q	3
number of inner MMA iterations per AL step, N_{MMA}	5
initial threshold projection penalization factor, β[b]	1
threshold projection density, η	0.5
initial guess, $\mathbf{z}^{(0)}$	0.5
tolerance, `tol`[c]	0.0015

[a]We use SIMP when neglecting self-weight and RAMP otherwise.
[b]Parameter β starts at 1 and increases by 0.5 every five AL steps and up to a maximum value of 15.
[c]We consider that the problem has converged when $\text{sum}(|\mathbf{z}^{(k+1)} - \mathbf{z}^{(k)}|) < \texttt{tol}$ and $\max(g_j) < 0.005$.

(a) Corbel design

This example studies the effect of the type of yield criterion on the optimized topology of a three-dimensional corbel whose geometry is shown in figure 4. The geometry is defined using $L = 1$ m, $t = 0.5$ m, and the load, P, is distributed over a distance, $d = 0.05$ m. The magnitude of the applied load is chosen appropriately depending on the material used for each design. For example, for designs made of ductile metals, which are defined by the von Mises or by the Tresca criteria, we use $P = 10\,000$ kN and for designs made of a cementitious material, we use $P = 600$ kN. The material properties and magnitude of the load, P, for each of the yield criteria, are summarized in table 3. All results reported in this example neglect the effects of self-weight. Moreover, for this example the domain is discretized using 250 000 regular hexahedral elements.

Figure 5 displays the topology optimization results obtained for each yield criterion. The results in figure 5*a*,*b* correspond to those obtained for the von Mises and Tresca criteria, respectively, for which the hydrostatic component of the Cauchy stress tensor has no effect. As a result, the optimized topologies become symmetric. Figure 5*c*–*f* displays the results for the Drucker–Prager, Mohr–Coulomb, Bresler–Pister and Willam–Warnke models, respectively, for which the hydrostatic component of the stress tensor is not negligible, yielding non-symmetric designs. The results from figure 5*c*–*f* show that, as compared to parts of the structure dominated by compressive stresses, those dominated by tensile stresses have thicker members. We also observe that for the Drucker–Prager criterion (figure 5*c*), regions with negative hydrostatic stresses (e.g. on the lower reentrant corner) result in necking. The reason for such behaviour is that, according to the Drucker–Prager criterion, no failure occurs under compressive hydrostatic stresses and, as as result, no material is needed in those regions. Despite the fact that we used different yield surfaces, all optimized structures from figure 5*c*–*f* share similarities. All those structures contain a thick member in tension that crosses by the upper reentrant corner, and thin compression members that meet at the lower reentrant corner. The members in compression are thinner than those in tension because, for all those cases, the compressive strength is larger than the tensile strength.

The results shown in figure 5*b*,*d* are obtained using a rounding parameter, $\zeta = 0.99$. In order to investigate the effect of ζ in the optimization results, figure 6 shows the optimized topologies

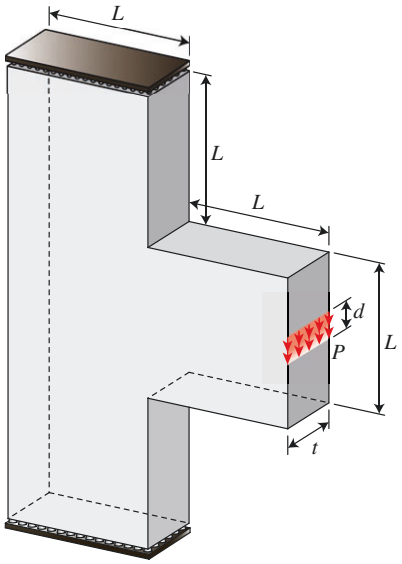

Figure 4. Geometry and loading for the corbel problem. The geometry is defined using $L = 1$ m and $t = 0.5$ m, and load P, whose magnitude depends on the yield criterion used to define material failure, is distributed uniformly across a distance $d = 0.05$ m. (Online version in colour.)

Table 3. Material properties and magnitude of the applied load used to solve the corbel problem.

	elastic properties		yield stress (MPa)				applied load
failure criterion	E (GPa)	ν	σ_{lim}	σ_t	σ_c	σ_b	P (kN)
von Mises and Tresca	200	0.3	250	—	—	—	10 000
Drucker–Prager and Mohr–Coulomb	30	0.2	—	10.5	35	—	600
Bresler–Pister and Willam–Warnke	30	0.2	—	10.5	35	52.5	600

obtained for the Tresca criterion using various values of ζ. The figures in the left column display the optimized topologies obtained for $\zeta = 0.95$ and 0.50, respectively, which show that the results are almost unaffected by the value of ζ. The figures in the centre column show the principal stresses measured at each evaluation point of the optimized structures (i.e. σ_i^e, $i = 1, 2, 3$, $e = 1, \ldots, N_e$), together with the rounded yield surfaces in principal stress coordinates for each of the designs. These results show that, independently of the value of ζ, all stress points are inside the yield surface (i.e. the stress constraints are satisfied locally). Finally, the figures in the right column show the yield surfaces as well as the principal stresses for each evaluation point when projected onto the deviatoric plane (i.e. the octahedral profile), which provide an additional view to show that the stress evaluation points lie inside the rounded Tresca yield surface.

(b) Dome design

This example investigates the effects of self-weight on the optimization results for a box domain whose geometry is shown in figure 7. The box domain is defined using $L = 10$ m and is subjected to a load of magnitude P applied at the centre and distributed uniformly on a circle of radius $r = 0.25$ m. The box is supported at its four lower corners by square rigid pads of dimension $d = 1$ m. In addition to considering self-weight, we also consider two yield criteria: von Mises (for a structure made of metal) and Willam–Warnke (for a structure made of a concrete-like material).

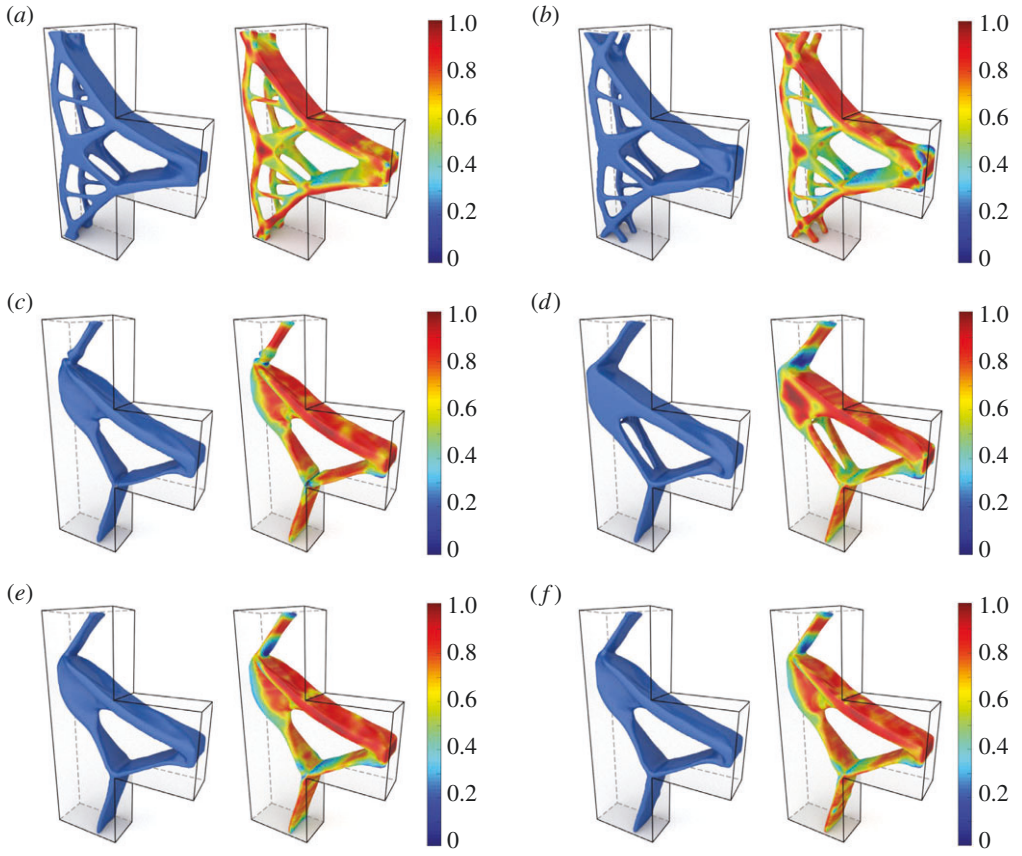

Figure 5. Optimized topologies (left) and equivalent stress measures (right) for the corbel problem using the unified failure criterion: (*a*) von Mises, (*b*) Tresca, (*c*) Drucker–Prager, (*d*) Mohr–Coulomb, (*e*) Bresler–Pister, and (*f*) Willam–Warnke. (Online version in colour.)

For the von Mises criterion, we use $E = 200\,\text{GPa}$, $\nu = 0.3$ and $\sigma_{\text{lim}} = 250\,\text{MPa}$ and for the Willam–Warnke criterion, we use $E = 30\,\text{GPa}$, $\nu = 0.2$, $\sigma_t = 7\,\text{MPa}$, $\sigma_c = 35\,\text{MPa}$ and $\sigma_b = 52.5\,\text{MPa}$. The box is discretized using 250 000 regular hexahedral elements.

To investigate the relative influence of the external load over the self-weight, we use the ratio P/W between the applied load, P, and the weight of the solid domain, W. The weight, W, corresponds to the total weight of the initial design domain, and it is computed as $W = \gamma L^3/4$, in which γ refers to the specific weight of the material. We obtain optimized topologies for four values of P/W ($P/W = -0.1$, $P/W = 0.01$, $P/W = 1$ and $P/W = \infty$). To obtain a similar volume fraction for all designs, we vary the magnitude of P for each P/W ratio. The magnitude of the applied load used to obtain each design is shown in table 4.

Figure 8 shows the results we obtain when using the von Mises criterion. When $P/W = -0.1$ (figure 8*a*), the load is applied in the upward direction and the optimized topology consists of four members connected to the four supports and a block of material underneath the point of load application. The block of material tries to counteract the effect of the upward load so that the overall mass of the structure is reduced. When $P/W = 0.01$ (figure 8*b*), the influence of self-weight is predominant, and the optimized topology contains a truss like structure that connects the point of load application to arch-like members located on the outer part of the domain to transfer the external load to the supports. When $P/W = 1$ (figure 8*c*) or $P/W = \infty$ (figure 8*d*), the influence of self-weight decreases, and the optimized topologies approach a truss. For these two cases, more

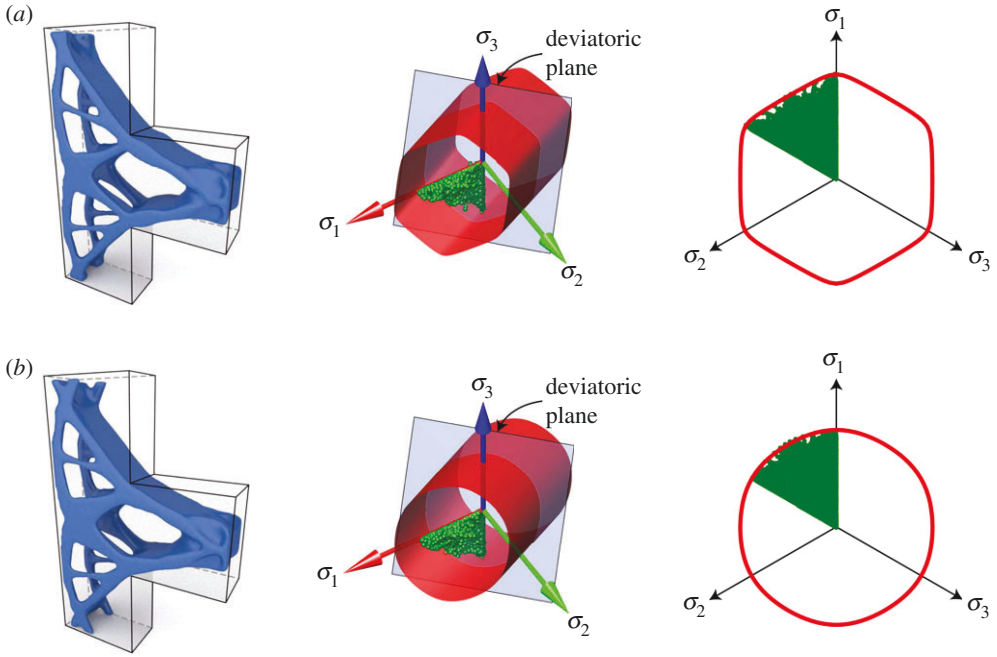

Figure 6. Optimized topologies (left), rounded Tresca yield surfaces (centre), and their projection onto the deviatoric plane (right), considering different values of the rounding parameter: (*a*) $\zeta = 0.95$ and (*b*) $\zeta = 0.50$. (Online version in colour.)

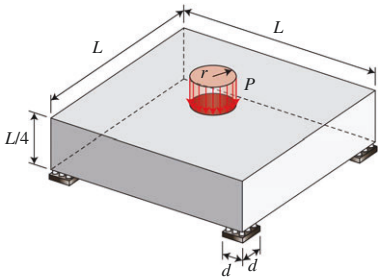

Figure 7. Geometry and loading for the dome problem. (Online version in colour.)

Table 4. Magnitude of the applied load, P, used to obtain the optimized topologies of figures 8 and 9 ($\times 10^3$ kN).

	P/W			
failure criterion	−0.1	0.01	1	∞
von Mises	−177	39	195	195
Willam–Warnke	−10.4	6	30	30

material appears underneath the point of load application, which is consistent from a structural point of view.

The results obtained using the Willam–Warnke criterion are displayed in figure 9. When the load is applied in the upward direction (i.e. when $P/W = -0.1$), the optimized topology

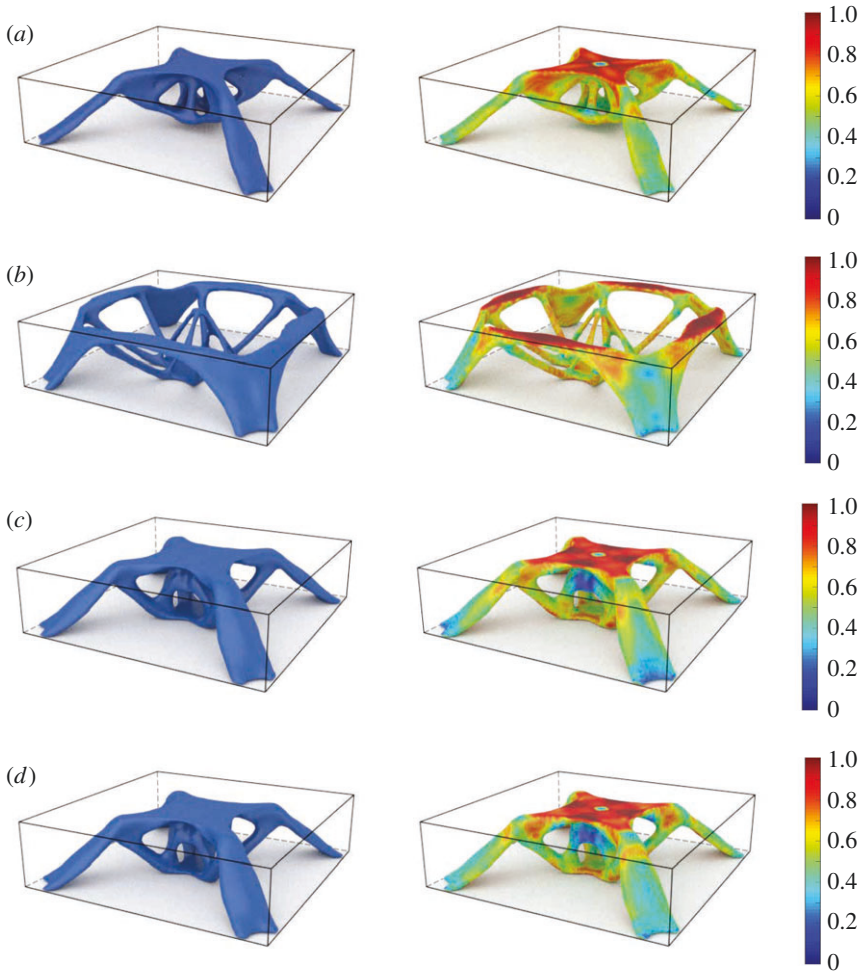

Figure 8. Optimized topologies (left) and equivalent stress measures (right) for the dome problem considering the von Mises yield criterion and various P/W ratios: (*a*) $P/W = -0.1$, (*b*) $P/W = 0.01$, (*c*) $P/W = 1$, and (*d*) $P/W = \infty$. (Online version in colour.)

becomes a truss-like structure (figure 9*a*) that bears resemblance to the structures shown in figures 8*c*,*d*. Due to the weakness of the material in tension, when $P/W = -0.1$ we increase the load application radius from $r = 0.25$ m to $r = 0.66$ m (cf. figure 7), which prevents the material from yielding at the point of load application. Now, when the effect of self-weight is dominant (i.e. when $P/W = 0.01$), the optimized topology corresponds to two arches that originate from the supports and intersect at the point of load application (figure 9*b*). Unlike the result in figure 8*b*, that obtained for the Willam–Warnke criterion only contains compressive members (i.e. the two intersecting arches). The reason for the difference in topology between these two results is that the material governed by the Willam–Warnke criterion is weak in tension and, as a result, the optimizer favours the appearance of materials that are subjected to compressive stresses. Now, when $P/W = 1$ (figure 9*c*) or when $P/W = \infty$ (figure 9*d*), the optimized topologies contain a bulky centre part and four compressive struts that connect each support with the point of load application. The bulky centre part appears so that the structure is able to bear with the complex state of stresses that develop underneath the point of load application. The bulky centre part helps increase the bearing capacity of the structure and the struts help transmit the load to the supports.

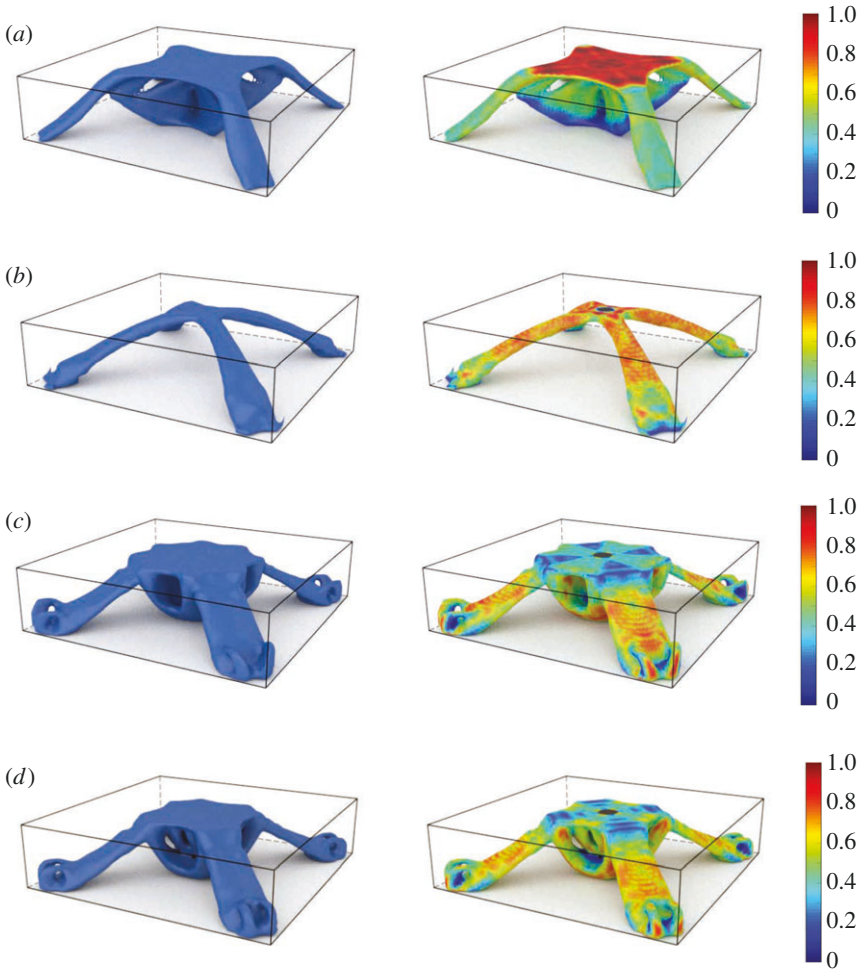

Figure 9. Optimized topologies (left) and equivalent stress measures (right) for the dome problem considering the Willam–Warnke yield criterion and various P/W ratios: (*a*) $P/W = -0.1$, (*b*) $P/W = 0.01$, (*c*) $P/W = 1$, and (*d*) $P/W = \infty$. (Online version in colour.)

6. Conclusions

In this paper, we demonstrate that several classical yield criteria, including von Mises, Drucker–Prager, Tresca, Mohr–Coulomb, Bresler–Pister and Willam–Warnke, can be defined using a single yield function, which we denote as the *unified yield function*. We use the unified yield function to solve mass minimization topology optimization problems with local stress constraints. To solve the problem with local constraints, we adopt an AL-based approach with a normalization that allows the solution of problems with a large number of constraints. The AL-based approach leads to the solution of the problem in a way that is consistent with continuum mechanics, i.e. treating stress as a local quantity. By virtue of the unified yield function, the formulation naturally extends the range of applications of stress-constrained topology optimization to structures that can be fabricated with a variety of materials ranging from ductile metals to pressure-dependent materials such as concrete, soils, ceramics, and polymeric foams, among others.

We consider the effects of self-weight and, more generally, those from design-dependent loading (e.g. centrifugal forces, electromagnetic body forces, among others). For problems involving self-weight, we use RAMP as the stiffness interpolation function, which helps prevent

numerical instabilities that arise in low density elements due to the unbounded ratio between mass and stiffness that occurs when SIMP is used. The results demonstrate that not only the choice of yield function but also the effects of self-weight are important to obtain an appropriate material layout via topology optimization.

Data accessibility. The online version of this article contains electronic supplementary material, which is available to authorized users.

Authors' contributions. G.H.P. designed the research. O.G.-L. and G.H.P conceived the mathematical models, interpreted computational results, analysed data and wrote the paper. O.G.-L. implemented the formulation and performed the simulations. All authors gave their final approval for publication.

Competing interests. We declare we have no competing interests.

Funding. This work was supported by the US National Science Foundation (NSF) under grant no. 1663244 and by the endowment provided by the Raymond Allen Jones Chair at the Georgia Institute of Technology.

Disclaimer. The information provided in this paper as well as the interpretation of the results is solely that by the authors, and it does not necessarily reflect the views of the sponsors or sponsoring agencies.

Acknowledgements. This paper is dedicated to the memory of Professor Daniel C. Drucker (1918–2001).[6] In addition, the authors would like to thank the anonymous reviewers for their valuable feedback, which helped to improve the quality and clarity of the manuscript.

Appendix A. Sensitivity analysis

We use a gradient-based optimization algorithm to solve the optimization problem (4.12), and thus, we require the sensitivity of the normalized AL function (4.24), which we obtain using the chain rule:

$$\frac{\partial J^{(k)}}{\partial z_j} = \sum_{i=1}^{N_e} \frac{\partial J^{(k)}}{\partial \tilde{\rho}_i} \frac{\partial \tilde{\rho}_i}{\partial \rho_i} \frac{\partial \rho_i}{\partial z_j} = \sum_{i=1}^{N_e} \frac{\partial J^{(k)}}{\partial \tilde{\rho}_i} \frac{\partial \tilde{\rho}_i}{\partial \rho_i} P_{ij}, \tag{A 1}$$

where

$$\frac{\partial \tilde{\rho}_i}{\partial \rho_i} = \frac{\beta[1 - \tanh(\beta(\rho_i - \eta))^2]}{\tanh(\beta\eta) + \tanh(\beta(1 - \eta))} \tag{A 2}$$

and P_{ij} is the filter matrix from equation (4.14). The sensitivity of the normalized AL function (4.24) with respect to the element volume fraction, $\tilde{\rho}_i$, is computed as

$$\frac{\partial J^{(k)}}{\partial \tilde{\rho}_i} = \frac{1}{|\Omega|} \frac{\partial}{\partial \tilde{\rho}_i} \sum_{e=1}^{N_e} \tilde{\rho}_e v_e + \frac{1}{N_c} \frac{\partial P^{(k)}}{\partial \tilde{\rho}_i} = \frac{v_i}{|\Omega|} + \frac{1}{N_c} \frac{\partial P^{(k)}}{\partial \tilde{\rho}_i}, \tag{A 3}$$

where

$$P^{(k)} = \sum_{j=1}^{N_c} \left[\lambda_j^{(k)} h_j(\mathbf{z}, \mathbf{u}) + \frac{\mu^{(k)}}{2} h_j(\mathbf{z}, \mathbf{u})^2 \right] \tag{A 4}$$

is the penalty term of the AL function. The sensitivity of the penalty term with respect to the element volume fractions is given by

$$\frac{\partial P^{(k)}}{\partial \tilde{\rho}_i} = \sum_{j=1}^{N_c} [\lambda_j^{(k)} + \mu^{(k)} h_j(\mathbf{z}, \mathbf{u})] \left[\frac{\partial h_j(\mathbf{z}, \mathbf{u})}{\partial \tilde{\rho}_i} + \frac{\partial h_j(\mathbf{z}, \mathbf{u})}{\partial \mathbf{u}} \cdot \frac{\partial \mathbf{u}}{\partial \tilde{\rho}_i} \right]. \tag{A 5}$$

We use the adjoint method to avoid computing the term $\partial \mathbf{u}/\partial \tilde{\rho}_i$ in (A 5), for which we use the equilibrium condition from equation $(4.12)_4$, which we rewrite in a convenient way as

$$\mathbf{R} = \frac{\partial \Pi}{\partial \mathbf{u}} + \epsilon \mathbf{u} = \mathbf{f}_{\text{int}} - \mathbf{f}_{\text{ext}} + \epsilon \mathbf{u} = \mathbf{0}, \tag{A 6}$$

[6]G.H.P. received the 2020 Drucker Medal from the American Society of Mechanical Engineers (ASME).

where $\mathbf{f}_{\text{int}}$ is the internal force vector, computed based on the strain energy of the system and $\mathbf{f}_{\text{ext}} = \mathbf{f}_n + \mathbf{f}_b$ is the external force vector. We add the term $\boldsymbol{\xi}^T(\partial\mathbf{R}/\partial\tilde{\rho}_i)$ to equation (A 5) and obtain

$$\frac{\partial P^{(k)}}{\partial\tilde{\rho}_i} = \sum_{j=1}^{N_c}[\lambda_j^{(k)} + \mu^{(k)}h_j(\mathbf{z},\mathbf{u})]\left[\frac{\partial h_j(\mathbf{z},\mathbf{u})}{\partial\tilde{\rho}_i} + \frac{\partial h_j(\mathbf{z},\mathbf{u})}{\partial\mathbf{u}}\cdot\frac{\partial\mathbf{u}}{\partial\tilde{\rho}_i}\right] + \boldsymbol{\xi}^T\left(\mathbf{K}_T\frac{\partial\mathbf{u}}{\partial\tilde{\rho}_i} + \frac{\partial\mathbf{f}_{\text{int}}}{\partial\tilde{\rho}_i} - \frac{\partial\mathbf{f}_b}{\partial\tilde{\rho}_i} + \epsilon\frac{\partial\mathbf{u}}{\partial\tilde{\rho}_i}\right), \tag{A 7}$$

where $\boldsymbol{\xi}$ is the adjoint vector and $\mathbf{K}_T$ is the tangent stiffness matrix at equilibrium. Here, we use the fact that the nodal force vector $\mathbf{f}_n$ is independent of the design variables and the body force vector $\mathbf{f}_b$ has a direct dependence on the design variables. We rewrite equation (A 7) by collecting all terms multiplying $\partial\mathbf{u}/\partial\tilde{\rho}_i$ and choose the adjoint vector $\boldsymbol{\xi}$ such that these terms vanish. After some algebraic manoeuvring, equation (A 7) simplifies to

$$\frac{\partial P^{(k)}}{\partial\tilde{\rho}_i} = \sum_{j=1}^{N_c}[\lambda_j^{(k)} + \mu^{(k)}h_j(\mathbf{z},\mathbf{u})]\frac{\partial h_j(\mathbf{z},\mathbf{u})}{\partial\tilde{\rho}_i} + \boldsymbol{\xi}^T\left(\frac{\partial\mathbf{f}_{\text{int}}}{\partial\tilde{\rho}_i} - \frac{\partial\mathbf{f}_b}{\partial\tilde{\rho}_i}\right), \tag{A 8}$$

where $\boldsymbol{\xi}$ solves the adjoint problem,

$$(\mathbf{K}_T + \epsilon\mathbf{I})\boldsymbol{\xi} = -\sum_{j=1}^{N_c}[\lambda_j^{(k)} + \mu^{(k)}h_j(\mathbf{z},\mathbf{u})]\frac{\partial h_j(\mathbf{z},\mathbf{u})}{\partial\mathbf{u}}. \tag{A 9}$$

Substitution of equation (A 8) into equation (A 3) yields

$$\frac{\partial J^{(k)}}{\partial\tilde{\rho}_i} = \frac{v_i}{|\Omega|} + \frac{1}{N_c}\left\{\sum_{j=1}^{N_c}[\lambda_j^{(k)} + \mu^{(k)}h_j(\mathbf{z},\mathbf{u})]\frac{\partial h_j(\mathbf{z},\mathbf{u})}{\partial\tilde{\rho}_i} + \boldsymbol{\xi}^T\left(\frac{\partial\mathbf{f}_{\text{int}}}{\partial\tilde{\rho}_i} - \frac{\partial\mathbf{f}_b}{\partial\tilde{\rho}_i}\right)\right\}, \tag{A 10}$$

which together with equation (A 1) leads to the sensitivity of the normalized AL function (4.24).

For the sake of completeness, we provide the expressions for the partial derivatives appearing in equations (A 9) and (A 10), which we require for the sensitivity analysis. First, we provide those appearing in equation (A 10). From equations (4.19) and (4.21), we have that $\partial h_j(\mathbf{z},\mathbf{u})/\partial\tilde{\rho}_i = 0$ whenever $g_j(\mathbf{z},\mathbf{u}) < -\lambda_j^{(k)}/\mu^{(k)}$ and

$$\frac{\partial h_j(\mathbf{z},\mathbf{u})}{\partial\tilde{\rho}_i} = \frac{\partial m_E(\rho_i)}{\partial\tilde{\rho}_i}\Lambda_j(\Lambda_j^2 + 1) \tag{A 11}$$

otherwise. To obtain $\partial\mathbf{f}_{\text{int}}/\partial\tilde{\rho}_i$, we recall that the material model is linear, and thus $\mathbf{f}_{\text{int}} = \mathbf{K}_T\mathbf{u}$. Therefore,

$$\frac{\partial\mathbf{f}_{\text{int}}}{\partial\tilde{\rho}_i} = \frac{\partial}{\partial\tilde{\rho}_i}(\mathbf{K}_T\mathbf{u}) = \frac{\partial m_E(\rho_i)}{\partial\tilde{\rho}_i}\mathbf{k}_0^i\mathbf{u}_i, \tag{A 12}$$

where $\mathbf{k}_0^i$ and $\mathbf{u}_i$ are the stiffness matrix (computed using the properties of the solid material) and the displacement vector of element i, respectively. Finally, we obtain the sensitivity of the body force vector, $\partial\mathbf{f}_b/\partial\tilde{\rho}_i$, from equation $(4.18)_2$, as follows:

$$\frac{\partial\mathbf{f}_b^e}{\partial\tilde{\rho}_i} = \frac{\partial m_V(\rho_i)}{\partial\tilde{\rho}_i}\mathbf{f}_{b0}^i, \quad \text{with } \mathbf{f}_{b0}^i = \int_{\Omega_i}\mathbf{N}_e^T\mathbf{b}\,\mathrm{d}\Omega. \tag{A 13}$$

Next, we proceed to provide the expression for the term $\partial h_j/\partial\mathbf{u}$ that appears in equation (A 9). Once more, the functional form of $h_j(\mathbf{z},\mathbf{u})$ in (4.21) shows that $\partial h_j(\mathbf{z},\mathbf{u})/\partial\mathbf{u} = \mathbf{0}$ whenever $g_j(\mathbf{z},\mathbf{u}) < -\lambda_j^{(k)}/\mu^{(k)}$ and

$$\frac{\partial h_j}{\partial\mathbf{u}} = \frac{\partial g_j}{\partial\mathbf{u}} = \frac{\partial g_j}{\partial\Lambda_j}\left(\frac{\partial\Lambda_j}{\partial I_1}\frac{\partial I_1}{\partial\boldsymbol{\sigma}} + \frac{\partial\Lambda_j}{\partial J_2}\frac{\partial J_2}{\partial\boldsymbol{\sigma}} + \frac{\partial\Lambda_j}{\partial J_3}\frac{\partial J_3}{\partial\boldsymbol{\sigma}}\right)\cdot\frac{\partial\boldsymbol{\sigma}}{\partial\mathbf{u}} \tag{A 14}$$

otherwise, where we use equation (4.19) to obtain the expression for $\partial g_j/\partial\mathbf{u}$ in equation (A 14). Recalling that $\Lambda_j = \sigma_j^{\text{eq}} - 1$, where the equivalent stress measure, σ_j^{eq}, is given by (3.1),

Table 5. Deviatoric function, $\hat{\alpha}(\theta)$, and modified Lode angle, $\hat{\theta}$, for classical yield criteria.

failure criterion	deviatoric function	modified Lode angle
von Mises	$\hat{\alpha}(\theta) = \dfrac{1}{\sigma_{\text{lim}}}$	$\hat{\theta} = \theta$
Drucker–Prager	$\hat{\alpha}(\theta) = \dfrac{\sigma_c + \sigma_t}{2\sigma_c\sigma_t}$	$\hat{\theta} = \theta$
Tresca[a]	$\hat{\alpha}(\theta) = \dfrac{2}{\sqrt{3}\sigma_{\text{lim}}}\cos\hat{\theta}$	$\hat{\theta} = \dfrac{1}{3}\sin^{-1}[\zeta \sin 3\theta]$
Mohr–Coulomb[a,b]	$\hat{\alpha}(\theta) = \dfrac{2\alpha}{3}\sqrt{3 + \left(\dfrac{\beta}{\alpha}\right)^2}\cos\hat{\theta}$	$\hat{\theta} = \dfrac{1}{3}\sin^{-1}[\zeta \sin 3\theta] + \tilde{\theta}$
Bresler–Pister[c]	$\hat{\alpha}(\theta) = \alpha_{\text{BP}}$	$\hat{\theta} = \theta$
Willam–Warnke[d]	$\hat{\alpha}(\theta) = \dfrac{A_{\text{W}}\cos^2\hat{\theta} + B_{\text{W}}}{C_{\text{W}}\cos\hat{\theta} + \sqrt{D_{\text{W}}\cos^2\hat{\theta} + E_{\text{W}}}}$	$\hat{\theta} = \theta + \dfrac{\pi}{6}$

[a] Setting $\zeta < 1$ leads to a yield surface with rounded corners [60].
[b] α and β are given by equation (2.13), and $\tilde{\theta}$ is given by equation (2.20).
[c] α_{BP} is given by equation (2.24).
[d] A_{W}, B_{W}, C_{W}, D_{W} and E_{W} are given by equation (2.32).

the sensitivity of the unified yield function with respect to the stress invariants is given by

$$\left.\begin{aligned} &\frac{\partial \Lambda_j}{\partial I_1} = \frac{\partial \sigma_j^{\text{eq}}}{\partial I_1} = \hat{\beta} + 2\hat{\gamma} I_1, \quad \frac{\partial \Lambda_j}{\partial J_2} = \frac{\partial \sigma_j^{\text{eq}}}{\partial J_2} = \frac{\partial \hat{\alpha}(\theta)}{\partial \theta}\frac{\partial \theta}{\partial J_2}\sqrt{3J_2} + \frac{3\hat{\alpha}(\theta)}{2\sqrt{3J_2}} \\ \text{and} \quad &\frac{\partial \Lambda_j}{\partial J_3} = \frac{\partial \sigma_j^{\text{eq}}}{\partial J_3} = \frac{\partial \hat{\alpha}(\theta)}{\partial \theta}\frac{\partial \theta}{\partial J_3}\sqrt{3J_2}, \end{aligned}\right\} \tag{A 15}$$

where the partial derivatives, $\partial\hat{\alpha}(\theta)/\partial\theta$, $\partial\theta/\partial J_2$ and $\partial\theta/\partial J_3$, are obtained from equations (3.2), (3.3) and (2.7).

The sensitivity of the stress invariants, I_1, J_2 and J_3, with respect to the vector of Cauchy stresses (written in Voigt notation) can be found explicitly. For instance, the first invariant of the Cauchy stress vector can be written as $I_1 = \mathbf{M}\boldsymbol{\sigma}$, with $\mathbf{M} = [1\ 1\ 1\ 0\ 0\ 0]$ and $\boldsymbol{\sigma} = [\sigma_{11}\ \sigma_{22}\ \sigma_{33}\ \sigma_{23}\ \sigma_{13}\ \sigma_{12}]^{\text{T}}$, and thus $\partial I_1/\partial\boldsymbol{\sigma} = \mathbf{M}^T$. Similarly, the second invariant of the deviatoric stress can be written as $J_2 = \frac{1}{3}\boldsymbol{\sigma}^T\mathbf{V}\boldsymbol{\sigma}$, where $\mathbf{V}$ is a 6×6 symmetric matrix, and thus $\partial J_2/\partial\boldsymbol{\sigma} = \frac{2}{3}\mathbf{V}\boldsymbol{\sigma}$. The third invariant of the deviatoric stress is obtained as

$$J_3 = s_{11}s_{22}s_{33} + 2\sigma_{23}\sigma_{13}\sigma_{12} - (s_{11}\sigma_{23}^2 + s_{22}\sigma_{13}^2 + s_{33}\sigma_{12}^2), \tag{A 16}$$

where $\mathbf{s} = [s_{11}\ s_{22}\ s_{33}\ s_{23}\ s_{13}\ s_{12}]^{\text{T}}$ is the deviatoric stress tensor expressed in Voigt notation. Thus,

$$\frac{\partial J_3}{\partial \boldsymbol{\sigma}} = \begin{bmatrix} s_{22}s_{33} - \sigma_{23}^2 \\ s_{11}s_{33} - \sigma_{13}^2 \\ s_{11}s_{22} - \sigma_{12}^2 \\ 2(\sigma_{13}\sigma_{12} - s_{11}\sigma_{23}) \\ 2(\sigma_{12}\sigma_{23} - s_{22}\sigma_{13}) \\ 2(\sigma_{23}\sigma_{13} - s_{33}\sigma_{12}) \end{bmatrix} + \frac{J_2}{3}\begin{bmatrix} 1 \\ 1 \\ 1 \\ 0 \\ 0 \\ 0 \end{bmatrix}. \tag{A 17}$$

The above expression for $\partial J_3/\partial\boldsymbol{\sigma}$ can also be found explicitly in [63]. The last two pieces needed to obtain $\partial h_j/\partial\mathbf{u}$ are $\partial g_j/\partial\Lambda_j$ and $\partial\boldsymbol{\sigma}/\partial\mathbf{u}$. The former is obtained from (4.19) and is given by $\partial g_j/\partial\Lambda_j = m_E(\tilde{\rho}_j)(3\Lambda_j^2 + 1)$. The latter is also found explicitly using the chain rule, $\partial\boldsymbol{\sigma}/\partial\mathbf{u} = \partial\boldsymbol{\sigma}/\partial\boldsymbol{\varepsilon} \cdot \partial\boldsymbol{\varepsilon}/\partial\mathbf{u} =$

Table 6. Equivalent stress measure, σ_{eq}, for classical yield criteria[a].

failure criterion	equivalent stress measure
von Mises and Tresca	$\sigma_{eq} = \hat{\alpha}(\theta)\sqrt{3J_2}$
Drucker–Prager and Mohr–Coulomb[b]	$\sigma_{eq} = \hat{\alpha}(\theta)\sqrt{3J_2} + \hat{\beta} I_1$
Bresler–Pister[c]	$\sigma_{eq} = \hat{\alpha}(\theta)\sqrt{3J_2} + \beta_{BP} I_1 + \gamma_{BP} I_1^2$
Willam–Warnke	$\sigma_{eq} = \hat{\alpha}(\theta)\sqrt{3J_2} + \dfrac{\sigma_b - \sigma_t}{3\sigma_b\sigma_t} I_1$

[a]The deviatoric function $\hat{\alpha}(\theta)$ for all yield criteria is given in table 5.
[b]$\hat{\beta} = (\sigma_c + \sigma_t)/2\sigma_c\sigma_t$ for Drucker–Prager and $\hat{\beta} = (\sigma_c + \sigma_t)/3\sigma_c\sigma_t$ for Mohr–Coulomb.
[c]β_{BP} and γ_{BP} are given by equation (2.24).

DB, where $\boldsymbol{\varepsilon}$ is the infinitesimal strain vector (in Voigt notation), **D** is the material tangent matrix and **B** is the strain-displacement matrix.

Appendix B. Summary of classical yield criteria

The unified yield function introduced in §3 is able to reproduce all classical yield criteria presented in §2. Table 5 presents explicit expressions for the deviatoric function, $\hat{\alpha}(\theta)$, used in equation (3.1) to define the unified yield function. All the analytical expressions for $\hat{\alpha}(\theta)$ shown in table 5 are derived from equation (3.2) and using the parameters displayed in table 1.

In a similar manner, table 6 presents explicit expressions for the equivalent stress measure, σ_{eq}, for all classical yield criteria considered in this study. All the analytical expressions for σ_{eq} shown in table 6 are derived from equation (3.1) and using the parameters displayed in table 1.

References

1. Duysinx P, Bendsœ MP. 1998 Topology optimization of continuum structures with local stress constraints. *Int. J. Numer. Methods Eng.* **43**, 1453–1478. (doi:10.1002/(SICI)1097-0207(19981230)43:8<1453::AID-NME480>3.0.CO;2-2)
2. Sved G, Ginos Z. 1968 Structural optimization under multiple loading. *Int. J. Mech. Sci.* **10**, 803–805. (doi:10.1016/0020-7403(68)90021-0)
3. Kirsch U, Taye S. 1986 On optimal topology of grillage structures. *Eng. Comput.* **1**, 229–243. (doi:10.1007/BF01200139)
4. Kirsch U. 1989 Optimal topologies in truss structures. *Comput. Methods Appl. Mech. Eng.* **72**, 15–28. (doi:10.1016/0045-7825(89)90119-9)
5. Kirsch U. 1990 On singular topologies in optimum structural design. *Struct. Optim.* **2**, 133–142. (doi:10.1007/BF01836562)
6. Rozvany GIN, Birker T. 1994 On singular topologies in exact layout optimization. *Struct. Optim.* **8**, 228–235. (doi:10.1007/BF01742707)
7. Yang RJ, Chen CJ. 1996 Stress-based topology optimization. *Struct. Optim.* **12**, 98–105. (doi:10.1007/BF01196941)
8. Duysinx P, Sigmund O. 1998 New developments in handling stress constraints in optimal material distribution. In *Proc. 7th AIAA/USAF/NASA/ISSMO Symp. on Multidisciplinary Analysis and Optimization, St Louis, MO, USA, 2–4 September 1998*, vol. 1, pp. 1501–1509. New York, NY: AIAA.
9. Luo Y, Wang MY, Kang Z. 2013 An enhanced aggregation method for topology optimization with local stress constraints. *Comput. Methods Appl. Mech. Eng.* **254**, 31–41. (doi:10.1016/j.cma.2012.10.019)
10. De Leon DM, Alexandersen J, Fonseca JS, Sigmund O. 2015 Stress-constrained topology optimization for compliant mechanism design. *Struct. Multidiscip. Optim.* **52**, 929–943. (doi:10.1007/s00158-015-1279-z)
11. Kiyono C, Vatanabe S, Silva E, Reddy J. 2016 A new multi-p-norm formulation approach for stress-based topology optimization design. *Compos. Struct.* **156**, 10–19. (doi:10.1016/j.compstruct.2016.05.058)

12. Lee K, Ahn K, Yoo J. 2016 A novel P-norm correction method for lightweight topology optimization under maximum stress constraints. *Comput. Struct.* **171**, 18–30. (doi:10.1016/j.compstruc.2016.04.005)
13. Lian H, Christiansen AN, Tortorelly DA, Sigmund O. 2017 Combined shape and topology optimization for minimization of maximal von Mises stress. *Struct. Multidiscip. Optim.* **55**, 1541–1557. (doi:10.1007/s00158-017-1656-x)
14. Liu H, Yang D, Hao P, Zhu X. 2018 Isogeometric analysis based topology optimization design with global stress constraint. *Comput. Methods Appl. Mech. Eng.* **342**, 625–652. (doi:10.1016/j.cma.2018.08.013)
15. Xia L, Zhang L, Xia Q, Shi T. 2018 Stress-based topology optimization using bi-directional evolutionary structural optimization method. *Comput. Methods Appl. Mech. Eng.* **333**, 356–370. (doi:10.1016/j.cma.2018.01.035)
16. Fan Z, Xia L, Lai W, Xia Q, Shi T. 2019 Evolutionary topology optimization of continuum structures with stress constraints. *Struct. Multidiscip. Optim.* **59**, 647–658. (doi:10.1007/s00158-018-2090-4)
17. Le C, Norato J, Bruns T, Ha C, Tortorelli D. 2010 Stress-based topology optimization for continua. *Struct. Multidiscip. Optim.* **41**, 605–620. (doi:10.1007/s00158-009-0440-y)
18. Lee E, James KA, Martins JRRA. 2012 Stress-constrained topology optimization with design-dependent loading. *Struct. Multidiscip. Optim.* **46**, 647–661. (doi:10.1007/s00158-012-0780-x)
19. Holmberg E, Torstenfelt B, Klarbring A. 2013 Stress constrained topology optimization. *Struct. Multidiscip. Optim.* **48**, 33–47. (doi:10.1007/s00158-012-0880-7)
20. Kreisselmeier G, Steinhauser R. 1979 Systematic control design by optimizing a vector performance index. *IFAC Proc. Vol.* **12**, 113–117. (doi:10.1016/S1474-6670(17)65584-8)
21. Park YK. 1995 Extensions of optimal layout design using the homogenization method. PhD thesis, University of Michigan, Ann Arbor.
22. Senhora FV, Giraldo-Londoño O, Menezes IFM, Paulino GH. 2020 Topology optimization with local stress constraints: a stress aggregation-free approach. *Struct. Multidiscip. Optim.* (doi:10.1007/s00158-020-02573-9)
23. Bertsekas DP. 1999 *Nonlinear programming*, 2nd edn. Belmont, MA: Athena Scientific.
24. Nocedal J, Wright SJ. 2006 *Numerical optimization*, 2nd edn. Berlin, Germany: Springer.
25. Izmailov AF, Solodov MV, Uskov EI. 2012 Global convergence of Augmented Lagrangian methods applied to optimization problems with degenerate constraints, including problems with complementarity constraints. *SIAM J. Optim.* **22**, 1579–1606. (doi:10.1137/120868359)
26. Andreani R, Haeser G, Schuverdt ML, Silva PJ. 2012 A relaxed constant positive linear dependence constraint qualification and applications. *Math. Program.* **135**, 255–273. (doi:10.1007/s10107-011-0456-0)
27. Pereira JT, Fancello EA, Barcellos CS. 2004 Topology optimization of continuum structures with material failure constraints. *Struct. Multidiscip. Optim.* **26**, 50–66. (doi:10.1007/s00158-003-0301-z)
28. Fancello EA. 2006 Topology optimization for minimum mass design considering local failure constraints and contact boundary conditions. *Struct. Multidiscip. Optim.* **32**, 229–240. (doi:10.1007/s00158-006-0019-9)
29. Emmendoerfer H Jr, Fancello EA. 2014 A level set approach for topology optimization with local stress constraints. *Int. J. Numer. Methods Eng.* **99**, 129–156. (doi:10.1002/nme.4676)
30. Emmendoerfer H Jr, Fancello EA. 2016 Topology optimization with local stress constraint based on level set evolution via reaction-diffusion. *Comput. Methods Appl. Mech. Eng.* **305**, 62–88. (doi:10.1016/j.cma.2016.02.024)
31. Emmendoerfer Jr H, Silva ECN, Fancello EA. 2019 Stress-constrained level set topology optimization for design-dependent pressure load problems. *Comput. Methods Appl. Mech. Eng.* **344**, 569–601. (doi:10.1016/j.cma.2018.10.004)
32. Da Silva GA, Beck AT, Cardoso EL. 2018 Topology optimization of continuum structures with stress constraints and uncertainties in loading. *Int. J. Numer. Methods Eng.* **113**, 153–178. (doi:10.1002/nme.5607)
33. da Silva GA, Beck AT, Sigmund O. 2019 Topology optimization of compliant mechanisms with stress constraints and manufacturing error robustness. *Comput. Methods Appl. Mech. Eng.* **354**, 397–421. (doi:10.1016/j.cma.2019.05.046)

34. da Silva GA, Beck AT, Sigmund O. 2019 Stress-constrained topology optimization considering uniform manufacturing uncertainties. *Comput. Methods Appl. Mech. Eng.* **344**, 512–537. (doi:10.1016/j.cma.2018.10.020)
35. von Mises R. 1913 Mechanik der festen Koerper in plastisch deformahlem Zustand. *Goettinger Narchrichten* **4**, 582–592.
36. Amstutz S, Novotny AA, de Souza Neto EA. 2012 Topological derivative-based topology optimization of structures subject to Drucker–Prager stress constraints. *Comput. Methods Appl. Mech. Eng.* **233**, 123–136. (doi:10.1016/j.cma.2012.04.004)
37. Bruggi M, Duysinx P. 2012 Topology optimization for minimum weight with compliance and stress constraints. *Struct. Multidiscip. Optim.* **46**, 369–384. (doi:10.1007/s00158-012-0759-7)
38. Luo Y, Kang Z. 2012 Topology optimization of continuum structures with Drucker–Prager yield stress constraints. *Comput. Struct.* **90**, 65–75. (doi:10.1016/j.compstruc.2011.10.008)
39. Bruggi M, Duysinx P. 2013 A stress–based approach to the optimal design of structures with unilateral behavior of material or supports. *Struct. Multidiscip. Optim.* **48**, 311–326. (doi:10.1007/s00158-013-0896-7)
40. Duysinx P, Van Miegroet L, Lemaire E, Brüls O, Bruyneel M. 2008 Topology and generalized shape optimization: why stress constraints are so important? *Int. J. Simul. Multidisci. Des. Optim.* **2**, 253–259. (doi:10.1051/ijsmdo/2008034)
41. Raghava R, Caddell RM, Yeh GS. 1973 The macroscopic yield behaviour of polymers. *J. Mater. Sci.* **8**, 225–232. (doi:10.1007/BF00550671)
42. Gali S, Dolev G, Ishai O. 1981 An effective stress/strain concept in the mechanical characterization of structural adhesive bonding. *Int. J. Adhesion Adhes.* **1**, 135–140. (doi:10.1016/0143-7496(81)90036-1)
43. Jeong SH, Park SH, Choi DH, Yoon GH. 2012 Topology optimization considering static failure theories for ductile and brittle materials. *Comput. Struct.* **110**, 116–132. (doi:10.1016/j.compstruc.2012.07.007)
44. Yoon GH. 2017 Brittle and ductile failure constraints of stress-based topology optimization method for fluid–structure interactions. *Comput. Math. Appl.* **74**, 398–419. (doi:10.1016/j.camwa.2017.04.015)
45. Tresca H. 1869 *Mémoire sur l'écoulement des corps solides*. Paris, France: Imprimerie Impériale.
46. Drucker DC, Prager W. 1952 Soil mechanics and plastic analysis for limit design. *Q. Appl. Math.* **10**, 157–165. (doi:10.1090/qam/48291)
47. Coulomb C. 1776 Essai sur une application des regles de maximis et minimis a quelques problemes de statique relatifs a l'architecture. *Mem. Acad. R. Div. Sav.* **7**, 343–387.
48. Bresler B, Pister KS. 1958 Strength of concrete under combined stresses. *ACI J.* **551**, 321–345.
49. Willam KJ, Warnke EP. 1975 Constitutive model for the triaxial behaviour of concrete. In *Proc. International Association for Bridge and Structural Engineering*, vol. 19, pp. 1–30.
50. Drucker DC. 1950 Some implications of work hardening and ideal plasticity. *Q. Appl. Math.* **7**, 411–418. (doi:10.1090/qam/34210)
51. Drucker D, Prager W, Greenberg H. 1952 Extended limit design theorems for continuous media. *Q. Appl. Math.* **9**, 381–389. (doi:10.1090/qam/45573)
52. Drucker DC. 1953 Coulomb friction, plasticity, and limit loads. Technical report. Providence, RI: Division of Applied Mathematics, Brown University.
53. Drucker DC. 1953 Limit analysis of two and three dimensional soil mechanics problems. *J. Mech. Phys. Solids* **1**, 217–226. (doi:10.1016/0022-5096(53)90001-5)
54. Drucker DC. 1956 On uniqueness in the theory of plasticity. *Q. Appl. Math.* **14**, 35–42. (doi:10.1090/qam/77386)
55. Drucker DC. 1957 A definition of stable inelastic material. Technical report. Providence, RI: Brown University.
56. Drucker DC. 1957 Soil mechanics and work-hardening theories of plasticity. *Trans. ASCE* **122**, 338–346.
57. National Academy of Engineering. 2015 *Memorial tributes*, vol. 19. Washington, DC: National Academies Press. (doi:10.17226/21785)
58. Lode W. 1926 Versuche über den Einfluß der mittleren Hauptspannung auf das Fließen der Metalle Eisen, Kupfer und Nickel. *Zeitschrift für Physik* **36**, 913–939. (doi:10.1007/BF01400222)
59. Crisfield MA. 1997 *Non-linear analysis of solids and structures*, vol. 2. New York, NY: Wiley.
60. Lagioia R, Panteghini A. 2016 On the existence of a unique class of yield and failure criteria comprising Tresca, von Mises, Drucker-Prager, Mohr-Coulomb, Galileo-Rankine, Matsuoka-Nakai and Lade-Duncan. *Proc. R. Soc. A* **472**, 20150713. (doi:10.1098/rspa.2015.0713)

61. Lade PV, Duncan JM. 1975 Lastoplastic stress-strain theory for cohesionless soil. *J. Geotech. Geoenviron. Eng.* **101**, 1037–1053.
62. Matsuoka H, Nakai T. 1974 Stress-deformation and strength characteristics of soil under three different principal stresses. *Proc. Jpn Soc. Civil Eng.* **232**, 59–70. (doi:10.2208/jscej1969.1974.232_59)
63. Abbo AJ, Sloan SW. 1995 A smooth hyperbolic approximation to the Mohr–Coulomb yield criterion. *Comput. Struct.* **54**, 427–441. (doi:10.1016/0045-7949(94)00339-5)
64. Gurtin ME. 1981 *An introduction to continuum mechanics*. Mathematics in Science and Engineering, vol. 158. New York, NY: Academic Press.
65. Wang F, Lazarov BS, Sigmund O. 2011 On projection methods, convergence and robust formulations in topology optimization. *Struct. Multidiscip. Optim.* **43**, 767–784. (doi:10.1007/s00158-010-0602-y)
66. Tikhonov AN, Arsenin VY. 1977 *Methods for solving ill-posed problems*. New York, NY: John Wiley and Sons.
67. Talischi C, Paulino GH. 2013 An operator splitting algorithm for Tikhonov-regularized topology optimization. *Comput. Methods Appl. Mech. Eng.* **253**, 599–608. (doi:10.1016/j.cma.2012.05.024)
68. Ramos A, Paulino G. 2016 Filtering structures out of ground structures—a discrete filtering tool for structural design optimization. *Struct. Multidiscip. Optim.* **54**, 95–116. (doi:10.1007/s00158-015-1390-1)
69. Bendsœ MP. 1989 Optimal shape design as a material distribution problem. *Struct. Optim.* **1**, 193–202. (doi:10.1007/BF01650949)
70. Zhou M, Rozvany GIN. 1991 The COC algorithm, Part II. Topological, geometrical and generalized shape optimization. *Comput. Methods Appl. Mech. Eng.* **89**, 309–336. (doi:10.1016/0045-7825(91)90046-9)
71. Rozvany GI, Zhou M, Birker T. 1992 Generalized shape optimization without homogenization. *Struct. Optim.* **4**, 250–252. (doi:10.1007/BF01742754)
72. Stolpe M, Svanberg K. 2001 An alternative interpolation scheme for minimum compliance topology optimization. *Struct. Multidiscip. Optim.* **22**, 116–124. (doi:10.1007/s001580100129)
73. Bruyneel M, Duysinx P. 2005 Note on topology optimization of continuum structures including self-weight. *Struct. Multidiscip. Optim.* **29**, 245–256. (doi:10.1007/s00158-004-0484-y)
74. Bourdin B. 2001 Filters in topology optimization. *Int. J. Numer. Methods Eng.* **50**, 2143–2158. (doi:10.1002/nme.116)
75. Cheng GD, Jiang Z. 1992 Study on topology optimization with stress constraints. *Eng. Optim.* **20**, 129–148. (doi:10.1080/03052159208941276)